
DIVIDE AND CONQUER: CLUSTER AND MANIFOLD-BASED INTERPRETATION OF COMPLEX FLOWS

A PREPRINT

 **Qihong L. Li-Hu**

Department of Aerospace Engineering
Universidad Carlos III de Madrid
Leganés, Madrid, Spain
qihonglorena.li@uc3m.es

 **Guy Y. Cornejo Maceda**

Department of Aerospace Engineering
Universidad Carlos III de Madrid
Leganés, Madrid, Spain

 **Andrea Ianiro**

Department of Aerospace Engineering
Universidad Carlos III de Madrid
Leganés, Madrid, Spain

 **Stefano Discetti**

Department of Aerospace Engineering
Universidad Carlos III de Madrid
Leganés, Madrid, Spain

January 9, 2026

ABSTRACT

We propose a framework for a global description of the dynamics of complex flows via clusterized spatial representations of the flow, isolating and identifying local dynamics, retrieving different Space-Time Cluster-Based Network Models (ST-CNMs). The key enabler is the partitioning of the domain based on a nonlinear manifold learning approach, in which spatial points are clustered based on the similarity of their dynamics, as observed in their compact embedding in manifold coordinates. The method receives as input time-resolved flow fields. From these, the spatial manifold is computed through isometric mapping applied to the vorticity time histories at each spatial location. An unsupervised clustering method, applied in the manifold space, partitions the full flow domain into subdomains. The dynamics of each subdomain are then described with cluster-based modeling. The method is demonstrated on two flow-field datasets obtained with a direct numerical simulation of a fluidic pinball under periodic forcing and with two-dimensional particle image velocimetry measurements of a transitional jet flow. The spatial manifold-based flow partitioning identifies regions with similar dynamics in an automated way. For both cases, ST-CNM identifies local dynamics that are not captured by a global approach. In particular, vortex shedding and vortex pairing dynamics are isolated in the jet flow experiment. The proposed fully automated domain partitioning method will benefit the structural description of controlled flows and unveil the actuation mechanisms at play.

Keywords Clustering · Manifold learning · ROM · POD · PIV

1 Introduction

This work proposes a framework for a simple, local, and interpretable description of complex flows through atomized views of the dynamics. Despite the recent developments and increase in computational power, the high complexity of the models and the prohibitively expensive numerical simulations still comprise a large bottleneck when modeling turbulent and complex flows. Moreover, obtaining interpretable descriptions of the flow is critical for modeling, design, and control applications to optimize the performance and efficiency of many devices. In other words, an interpretable description of the flow consists of providing its structural organization, i.e., the identification of different flow regions such as mixing layers or recirculation zones, of the main coherent features in each region, and of the regions of strong nonlinear interaction, including vortex tilting, stretching, and merging. Characterizing these coherent structures

and their intrinsic dynamics is essential for flow estimation and prediction. Understanding their origin and evolution is thus indispensable for flow design and control. In closed-loop control, the localization of these structures and their evolution under forcing is fundamental for sensor and actuator placement, and for deriving actuation strategies targeting the dominant dynamical degrees of freedom. Moreover, in the era of machine-learning flow control [Duriez et al., 2017, Rabault et al., 2019, Brunton et al., 2020], where control laws or agents are often learned without explicit physical prior, an automated physical interpretation of the learned solutions is needed. For instance, the description of the evolution of coherent structures under actuation is essential to unveil the mechanisms discovered by the learning algorithm and to enable generalization across different operating conditions and geometries.

The modeling of complex flows is challenged by their multiscale character, broadband frequency content, and intricate nonlinear interactions. Such features hinder the construction of Reduced-Order Models (ROMs) that remain faithful, stable, and interpretable across regimes. With the increase in computational power and the development of advanced experimental diagnostics, data-driven modeling has emerged as a compelling alternative for extracting structure from high-dimensional flow fields. Proper Orthogonal Decomposition (POD) [Lumley, 1967] has been widely used for this purpose, yet at high Reynolds numbers, the wide range of spatial and temporal scales necessitates a large number of modes, reducing interpretability. Projection-based reduced-order models built from such bases often become computationally expensive and exhibit complex nonlinear modal interactions that obscure physical insight [Li-Hu et al., 2025]. Methods designed to promote dynamical relevance, such as Spectral Proper Orthogonal Decomposition (SPOD) [Towne et al., 2018], Dynamic Mode Decomposition (DMD) [Schmid, 2010], or multiscale POD [Mendez et al., 2019], provide frequency- or time-scale-specific modes but rely on prior assumptions about the dominant time scales and do not naturally yield spatially localized structures. Autoencoders offer a flexible approach for nonlinear dimensionality reduction and prediction, but the learnt latent variables and decoder modes usually remain difficult to interpret. Cluster-based modeling [Kaiser et al., 2014, Li et al., 2021, Fernex et al., 2021, Deng et al., 2022, Hou et al., 2022, 2024] has proven effective in identifying quasi-attractors and transition processes by partitioning the trajectory in time. However, global clustering approaches are not naturally suited for resolving spatially localized coherent structures without introducing a prohibitively large number of clusters.

A promising approach to improve the fidelity and interoperability of models is to partition the data into coherent subsets, yielding local models. The partitioning can be performed in the phase space and combined with intrusive model methods [Colanera and Magri, 2025], in the sequence of snapshots combined with non-intrusive methods [Geelen and Willcox, 2022, Deng et al., 2025], and in the spatial domain. Spatially local approaches have recently been shown to improve generalizability and to reduce computational cost compared to full-domain models [Farcas et al., 2024, Xu et al., 2025]. Domain partitioning has been used in Computational Fluid Dynamics (CFD) to reduce computational cost, either through manual subdivision exploiting problem symmetries [Farcas et al., 2024] or through criteria that define boundaries between regions of distinct dynamical behavior. Examples include decompositions based on error indicators that distinguish low- and high-fidelity regions [Bergmann et al., 2018], and partitioning according to the decay of singular values to build locally coupled models [Gkimisis et al., 2025]. Finally, extended physics-informed neural networks (XPINNs) [Jagtap and Karniadakis, 2020]—the domain-partitioned version of PINNs—outperforms classical PINNs in terms of generalization and convergence speed for the modelization of multiscale and multiphysics problems [Hu et al., 2022].

Supervised and unsupervised machine learning methods have also been employed to decompose the domains. Supervised methods aim to partition the domain based on a given flow characteristic. For instance, Li et al. [2020] trains a detector in a supervised way to separate turbulent and non-turbulent regions. On the other hand, unsupervised flow partition aims to automatically extract relevant flow features. These approaches rely on the definition of a metric between spatial points that defines a feature space where the dynamics of the flow are separated. Those clustering features have been defined in several ways. For example, Callaham et al. [2021] propose a clustering based on an equation space to identify local balances. Similarly, Otmani et al. [2023, 2025] separate viscous and turbulent regions using invariants of the strain-rate and rotation tensors. Parente et al. [2009] proposes another approach based on vector quantized principal component analysis (VQPCA) [Kambhatla and Leen, 1997], where the metric is defined as the reconstruction error of the local time series. Muñoz et al. [2023] compare different reduced order modeling methods (e.g., POD, autoencoders) and show that VQPCA achieves the lowest reconstruction error. Overall, the resulting domain partitioning obtained from these methods is expected to depend on the physics embedded in the features. Here, we propose a least-biased partitioning of the domain, i.e., based on snapshot data and with minimal human intervention.

In the light of literature, the scientific gap we aim to fulfill is a least-biased interpretation of complex flows. To this end, we introduce an unsupervised domain partitioning method to model the flow based on a space-time clustering of snapshot data. First, the domain is partitioned within a feature space (*spatial manifold*) constructed from local time-series signatures of the flow field with isometric mapping (ISOMAP) [Tenenbaum et al., 2000]. The novelty compared to previous studies lies in the definition of the features based on a nonlinear dimensionality reduction method. Under the manifold hypothesis, high-dimensional flow data can be assumed to lie near a lower-dimensional structure param-

eterized by spatially varying local dynamics. Clustering within this spatial manifold yields an atomized representation of the dynamics, enabling the identification of spatially localized coherent structures and their local evolution. Second, each subdomain is described with local Markov models based on cluster-based network modeling [Li et al., 2021, Fernex et al., 2021]. The proposed method is demonstrated for two statistically stationary flows, a numerical simulation of the fluidic pinball under control [Deng et al., 2020, Cornejo Maceda et al., 2021] and an experimental jet flow at Reynolds number $Re = 3300$ [Franceschelli et al., 2025].

The manuscript is organized as follows. First, the spatial and temporal clustering methodology is presented in §2. Next, the controlled local dynamics of the fluidic pinball are analyzed in §3. Then, an experimental jet flow is studied in §4. Finally, §5 summarizes the results and offers concluding remarks.

2 Methodology

This section details the methodology of the ST-CNM. First, an overview of the method is presented (§2.1). The domain decomposition and local cluster-based modeling are further explained in §2.2 and §2.3.

2.1 Overview

Figure 1 illustrates the three main steps of the methodology.

- (a) The starting point is time-resolved and spatially-resolved snapshot data, typically obtained from numerical simulations or experimental measurements, such as Particle Image Velocimetry (PIV).
- (b) Then, the flow is partitioned in an unsupervised way into non-overlapping subdomains.
- (c) Finally, each subdomain is described with local Markov models with Cluster-based Network Models (CNMs).

The spatial partitioning step aims to separate regions based on local dynamics, so that regions with similar behaviour are assigned to the same subdomain. The aim is to derive a dynamic-based partitioning enabling the derivation of simple local models for each region. The domain decomposition is carried out by first defining a feature space where two points with similar dynamics are close. This space is built with an analysis of each grid point based on ISOMAP, which is spanned by the coordinates γ_1 , γ_2 , and γ_3 in figure 1. The dimension of this space is determined by the minimum residual variance. Note that each point in this reduced space represents a point in the domain. The shape described by all the points is referred to as *spatial manifold*. Then, a clustering algorithm is employed to partition the spatial manifold, and the affiliation function of each cluster is employed to partition the flow field into subdomains. Note that the subdomains are not necessarily connected in the physical space.

To describe the dynamics of each subdomain, a temporal partitioning of the flow data is performed, where the snapshots correspond to the flow fields representing either the full domain or a subdomain. For this, the cluster-based network modeling from Li et al. [2021] and Fernex et al. [2021] is employed. First, the snapshots are partitioned into *subsequences* with a clustering algorithm. The subsequences correspond to the clusters defined in Li et al. [2021], and refer to a set of snapshots, without any specific ordering. This term is chosen here to avoid any confusion with the clusters obtained in the spatial partitioning step, also referred to as a subdomain. In the following, the term subdomain is employed exclusively for the spatial clusters. On the other hand, subsequence and cluster are used interchangeably for the classic temporal clusters. Note that the clustering of the snapshots is equivalent to the clustering of the temporal POD modes. In practice, the POD modes are preferred for their alleviated computational load [Kaiser et al., 2014]. Then, the transition probability matrix and transition time matrix are built based on the number of snapshots that leave from one subsequence to another and the residence time in each subsequence, respectively. The first one describes a Markovian and stochastic transition of the flow from one subsequence to another, while the latter gives the average transition time from one subsequence to another. To model the dynamics, each subsequence is approximated by its centroid. The validity of the model is tested by comparing the autocorrelation functions of the original flow and the predicted flow, obtained by sampling a new trajectory using the transition matrices from an initial centroid. The time information is obtained from the transition time matrix, where the original time resolution is recovered by linear interpolation between successive centroids.

Before detailing the methodology of each step, we clarify the distinction between the space clustering performed in the first step —figure 1(b)— and the time clustering in the second step —figure 1(c). Clustering consists of partitioning a set of observations into clusters based on their similarity. Without loss of generality, observations are described as vectors in an n -dimensional space, and the similarity between two vectors is measured by a prescribed metric, often based on the inner product of the space. Finally, the clustering provides an affiliation function that, for each observation, retrieves its corresponding cluster.

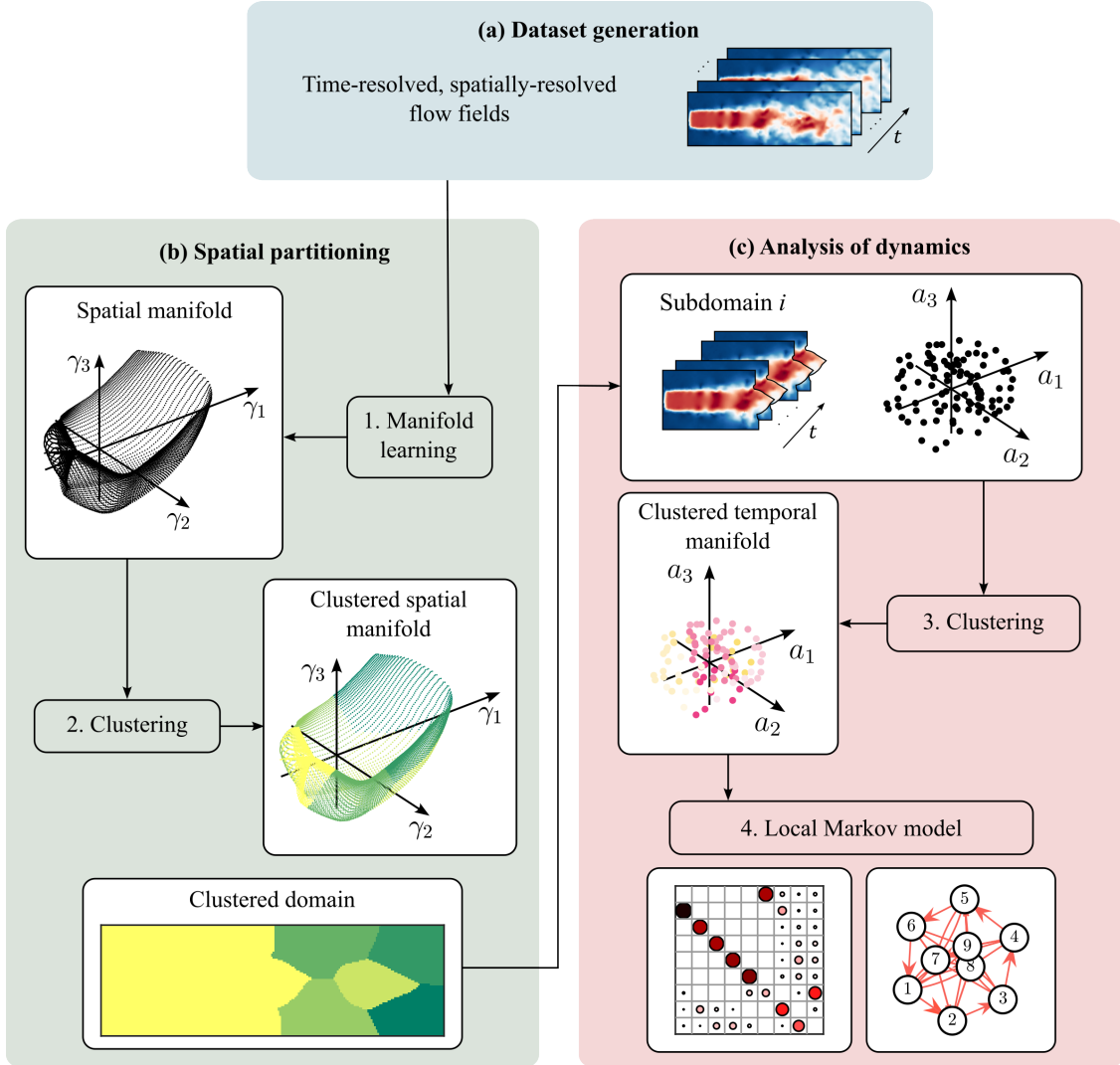


Figure 1: Schematics of the space-time cluster-based network model methodology. (a) Starting point is time-resolved velocity field snapshot data. The core idea being building a *spatial manifold*, i.e., deriving a set of coordinates where two points with similar dynamics are close to each other. γ_i correspond to the spatial manifold coordinates. The domain is then partitioned into subdomains with a clustering method applied to these spatial coordinates. (c) Cluster-based kinematic models are built for each subdomain i , represented with cropped velocity field snapshots. The atomized domain aids a simple interpretation of the dynamics. a_i correspond to the temporal modes of the flow fields.

For the spatial partitioning, one observation is the time sequence of a physical quantity at a given point in space. When several quantities are considered, e.g., u , v , and w components of a 3D flow, they are all concatenated to form one long sequence. A cluster is a set of time sequence vectors, corresponding to several points in space. The affiliation function is then employed to assign each space to a subdomain. Contrary to the classic temporal clustering, the centroids of a space cluster do not have, a priori, a physical interpretation. Instead, they consist of the averaged time sequence of a physical quantity that includes phase shifts. Note that temporal resolution is not required to compute the distance between time series; thus, this partitioning strategy can be applied to non-time-resolved data.

On the other hand, for the time partitioning of the data, each observation is a snapshot at a given time. A cluster is a set of snapshots at different times, and its centroid is the average flow field across all snapshots in the cluster. The centroid corresponds to a representative realization of the flow. This clustering corresponds to the one introduced by Kaiser et al. [2014]. To avoid any confusion between the time and space clustering, the space clusters are referred to as subdomains, while the time clusters are referred to as subsequences.

2.2 Dynamics-based spatial partitioning

This subsection describes the spatial partitioning of the flow.

Let's consider N_t time- and space-resolved snapshots $\{\mathbf{u}(\mathbf{x}, t_k)\}_{1 \leq k \leq N_t}$ of a velocity field. We consider here a two-dimensional flow field for clarity, without loss of generality. The velocity field is discretized on the grid defined by N_s points $\mathbf{x}_i = (x_i, y_i) \in \mathbb{R}^2$. The goal of the spatial partition is to derive non-trivial subsets of spatial points that cover the whole domain and whose intersection is empty. A dynamics-based spatial partitioning aims to derive a spatial partitioning where points with similar dynamics are in the same subset. The dynamics of each point is described by the time series of each physical quantity. Following the clustering terminology, each point in space is an observation, and its associated time series is its features.

In this work, a vorticity time series is selected as the feature for each point as it synthesizes both velocity components into a single quantity, thus alleviating the computational load. The data matrix is then described as:

$$\mathbf{W} = \begin{bmatrix} \omega(\mathbf{x}_1, t_1) & \omega(\mathbf{x}_2, t_1) & \cdots & \omega(\mathbf{x}_{N_s}, t_1) \\ \omega(\mathbf{x}_1, t_2) & \omega(\mathbf{x}_2, t_2) & \cdots & \omega(\mathbf{x}_{N_s}, t_2) \\ \vdots & \vdots & \ddots & \vdots \\ \omega(\mathbf{x}_1, t_{N_t}) & \omega(\mathbf{x}_2, t_{N_t}) & \cdots & \omega(\mathbf{x}_{N_s}, t_{N_t}) \end{bmatrix}. \quad (1)$$

Then, ISOMAP is employed to define a space where two points are close to each other if their corresponding time series are close. ISOMAP consists of a nonlinear data decomposition method that aims to extract a few coordinates that describe the dataset and conserves the geodesic distance between the points. ISOMAP has been recently employed in fluid mechanics to extract low-dimensional manifolds of the flow dynamics [Farzamnik et al., 2023, Marra et al., 2024]. In this work, ISOMAP is employed to construct a spatial manifold that maps the different types of dynamics in the flow.

The Euclidean distance $d_{i,j}$ between two time series $\omega_i = \omega(\mathbf{x}_i)$ and $\omega_j = \omega(\mathbf{x}_j)$ is computed according to:

$$d_{i,j} = \int_0^T (\omega_i(t) - \omega_j(t))^2 dt. \quad (2)$$

where $\mathbf{D} = [d_{i,j}]_{1 \leq i,j \leq N_s}$ is the distance matrix. Then, the manifold coordinates of the data are extracted with ISOMAP. The algorithm structure is briefly detailed here:

1. **Build data network.** A network between the data points is built by considering the k nearest neighbors. For each snapshot, the k nearest neighbors are identified.
2. **Compute geodesic distance.** The geodesic distance between two points is computed as the shortest path in the network. If two snapshots are neighbors, their distance corresponds to the Euclidean distance; otherwise, the shortest path is identified with the Floyd algorithm [Floyd, 1962]. The resulting geodesic distance matrix is noted \mathbf{D}_G .
3. **Compute ISOMAP coordinates.** Multidimensional Scaling (MDS) [Torgerson, 1952] is applied to \mathbf{D}_G to extract a set of coordinates. In short, the matrix \mathbf{D}_G is double-centered and diagonalized, with eigenvectors w_i and eigenvalues λ_i .
4. **Select number of coordinates.** The vector containing the i -th manifold coordinate of the points is defined as $\gamma_i = \sqrt{\lambda_i} w_i$. In the following, the i -th dimension of the manifold is noted γ_i (not bold). Following

Tenenbaum et al. [2000], the number of dimensions retained is given by analyzing the residual variance

$$R_v(n) = 1 - R^2(\text{vec}(\mathbf{D}_G), \text{vec}(\mathbf{D}_n)), \quad (3)$$

where $R(\cdot, \cdot)$ is the correlation coefficient, $\text{vec}(\cdot)$ is the vectorization operator, and \mathbf{D}_n is the matrix of the Euclidean distances between the points in the manifold coordinates system, retaining only the first n coordinates.

We refer to Marra et al. [2024] for more information on the ISOMAP methodology. The number of dimensions is chosen as the first minimum of $R_v(n)$, and the corresponding n -dimensional manifold extracted is referred to as the spatial manifold.

Each spatial point is represented by n coordinates. These coordinates are the features employed for clustering, which is carried out by the k -means++ algorithm [Arthur and Vassilvitskii, 2007]. k -means takes as input the number of clusters N_c and computes iteratively N_c centroids that define a Voronoi tessellation of the n -dimensional space. Starting from the given N_c initial centroids \mathbf{c}_i , the algorithm assigns each observation (in this case, each spatial point) to the closest centroid. A set of data points, also known as a cluster, is then created for each centroid. The cluster i associated to centroid \mathbf{c}_i is noted \mathcal{C}_i . Then, the centroids are updated as the average within each cluster, and the algorithm is iterated until convergence. The variant k -means++ optimizes the initial centroids to maximize the distance between each other.

The number of clusters is decided according to the Two-Line Fit (TLF) method [Brindise and Vlachos, 2017]. This method consists of sweeping a large range of values and identifying the value that best splits the evolution of the explained variance into two linear segments. First, the data is clustered for a large range of values, and the explained variance is computed. The explained variance for N_c clusters is defined as:

$$E_v(N_c) = 1 - \frac{\text{WCSS}(N_c)}{\text{WCSS}(1)} \quad (4)$$

where $\text{WCSS}(N_c)$ is the within-cluster sum of squares for N_c clusters:

$$\text{WCSS}(N_c) = \sum_{k=1}^{N_c} \frac{1}{|\mathcal{C}_k|} \sum_{\mathbf{z} \in \mathcal{C}_k} \|\mathbf{z} - \mathbf{c}_k\|^2.$$

The number of clusters is typically computed until the convergence of the explained variance. For the configurations considered in this work, the clustering is performed up to 50 clusters. Then, for a given number N_c of clusters, the evolution of the explained variance is split in two parts, and the lower and upper parts are fit with linear functions. The optimal number of clusters is chosen as the value that maximizes the ratio R^2/ϵ , where R^2 is the averaged coefficient of determination and ϵ is the prediction error defined as the sum of the difference between the predicted and the original values. In the context of domain partitioning, the resulting clusters are referred to as subdomains and noted \mathcal{D}_i .

No meta-parameter tuning is required in the spatial partitioning presented in this section, with the exception of the number of neighbors needed in ISOMAP. Nonetheless, this parameter is expected to have a limited influence on the resulting manifold as long as the value is not so high that it causes a short-circuit in the neighboring network.

2.3 Local cluster-based network model

Once the domain is partitioned, a cluster-based network model [Li et al., 2021] is built for each subdomain. The methodology follows the steps of the original paper, i.e., (1) clustering of the snapshots, (2) computation of the direct transition probability matrix and the transition time matrix. Note that in this section, clustering corresponds to a partitioning of the snapshots, namely, extracting subsequences of snapshots based on their similarities. In this context, the observations are the snapshots and the features are the u and v components of the velocity at each point of the subdomain. In short, the data is viewed as N_t observations with $2 \times N_{s,i}$ features each, where $N_{s,i}$ is the number of points in subdomain i .

Based on this description of the data, clustering is performed in the same way as in §2.2. The metric between two snapshots \mathbf{u} and \mathbf{v} is then based on the inner product defined on the Hilbert space $\mathcal{L}^2(\mathcal{D}_i)$ of square-integrable vector fields in the domain \mathcal{D}_i ,

$$(\mathbf{u}, \mathbf{v})_{\mathcal{D}_i} := \int_{\mathcal{D}_i} \mathbf{u} \cdot \mathbf{v} \, dx. \quad (5)$$

As mentioned in §2.1, the clustering can also be carried out on the temporal POD modes. In this case, the features of each observation are the temporal POD modes a_i . In other words, for the k -th observation, corresponding to snapshot

$\mathbf{u}(\mathbf{x}, t_k)$, the features are $\mathbf{a}_k = (a_i(t_k))$, Note that the temporal POD modes describe a “temporal” manifold where the dynamics of the flow evolve. The resulting clusters are referred to as subsequences and noted \mathcal{S}_j . The associated centroids are noted \mathbf{s}_j . We recall that \mathbf{s}_j is a snapshot as an average of the snapshots in \mathcal{S}_j . Similarly to §2.2, the number of subsequences is chosen with the TLF criterion.

The direct transition probability \mathbf{Q} and transition time matrices \mathbf{T} are then computed. The transition probability from \mathcal{S}_j to \mathcal{S}_i is:

$$Q_{ij} = \frac{n_{ij}}{n_j} \quad (6)$$

where n_{ij} is the number of snapshots in \mathcal{S}_j whose immediate successor in the original sequence is in \mathcal{S}_i , and n_j is the number of snapshots in \mathcal{S}_j whose immediate successor in the original sequence is no longer in \mathcal{S}_j . The transition time from \mathcal{S}_j to \mathcal{S}_i is

$$T_{ij} = \langle \frac{\tau_i + \tau_j}{2} \rangle \quad (7)$$

where τ_j is the residence time in \mathcal{S}_j , i.e., the number of successive snapshots times in \mathcal{S}_j for a trajectory, and $\langle \cdot \rangle$ denotes the ensemble average over all trajectories.

The flow field data is then reconstructed by sampling a sequence of clusters from the transition probability matrix \mathbf{s}_{k_0} , \mathbf{s}_{k_1} , \mathbf{s}_{k_2} , etc., where now k_i refers to the index of the temporal cluster. The time information is retrieved with the transition time matrix: $t_0 = 0$, $t_1 = T_{k_1 k_0}$, $t_2 = t_1 + T_{k_2 k_1}$, etc. The reconstructed velocity field at $t \in [t_n, t_{n+1}]$ is then:

$$\begin{aligned} \hat{\mathbf{u}}(\mathbf{x}, t) &= \alpha_n \mathbf{s}_{k_n}(\mathbf{x}) + (1 - \alpha_n(t)) \mathbf{s}_{k_{n+1}}(\mathbf{x}) \\ \alpha_n &= \frac{t_{n+1} - t}{t_{n+1} - t_n} \end{aligned} \quad (8)$$

Similar to Li et al. [2021], the validity of the local cluster-based network models is verified with the autocorrelation function of the velocity field [Protas et al., 2015]:

$$R(\tau) = \frac{1}{T - \tau} \int_{\tau}^T \int_{\mathcal{D}_i} \mathbf{u}(\mathbf{x}, t - \tau) \cdot \mathbf{u}(\mathbf{x}, t) d\mathbf{x} dt, \quad \tau \in [0, T) \quad (9)$$

For more details on the cluster-based network modeling, we refer to Li et al. [2021].

3 Flow description of the fluidic pinball under control

The ST-CNM methodology is first demonstrated for a two-dimensional numerical dataset of a flow under control action, the fluidic pinball. The flow is forced at different incommensurable frequencies to mimic a multi-frequency flow.

3.1 Configuration

Figure 2 depicts the fluidic pinball configuration as described in the work by Deng et al. [2020]. The system consists of three cylinders located at the vertices of an equilateral triangle pointing upstream. The diameter of the cylinders is noted as D . The centers of the cylinders are located at $3D/2$ of each other. The flow is described in a Cartesian coordinate system. The origin is located halfway between the two rear cylinders. The x -axis is oriented with the direction of the incoming flow. The y -axis is chosen such that the angle from the x - to the y -axis points counter-clockwise. The flow domain extends $20D$ downstream, $6D$ upstream, and $12D$ spanwise.

We consider an incompressible flow at $Re = U_{\infty} D / \nu = 30$, where U_{∞} is the incoming velocity, and ν the kinematic viscosity of the fluid. The density of the fluid is noted as ρ . All quantities are normalized by the D , U_{∞} and ρ . At this Reynolds number, the flow is beyond the first Hopf bifurcation and the only attractor in the phase space is a symmetric limit cycle [Deng et al., 2020]. Periodic vortex shedding forming a von Kármán vortex street is observed. The non-dimensional frequency of the unforced vortex shedding is $f_0 = 0.088$ and the corresponding period $T_0 = 11.36$, normalized with the convective time.

The flow is studied through direct numerical simulations of the incompressible Navier-Stokes equations. The numerical simulations are carried out with an in-house solver validated in the works by Deng et al. [2020] and Noack et al. [2003]. The Navier-Stokes equations are solved based on a second-order finite element discretization method on an unstructured grid of 4225 triangles and 8633 vertices, see figure 2a. The method is third-order accurate in time and

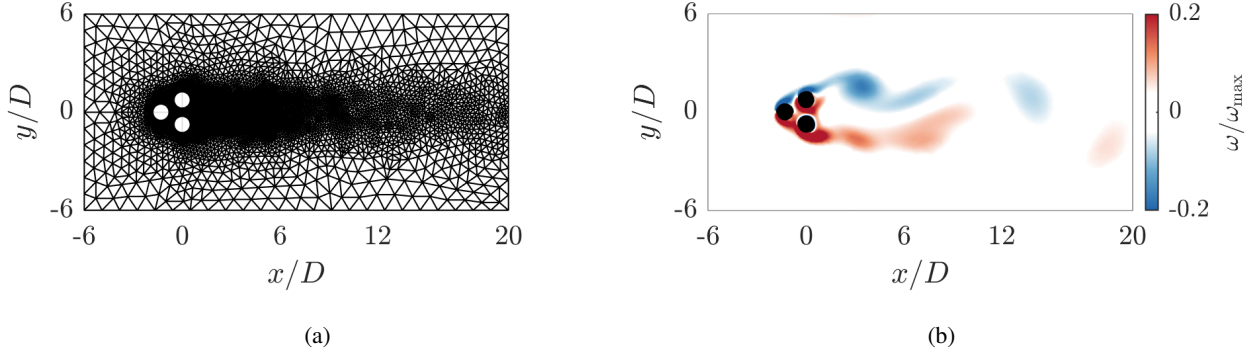


Figure 2: Fluidic pinball configuration. (a) Computational grid. (b) Vorticity field of a sample snapshot of the flow under control.

space. The velocity is set to $\mathbf{u} = (U_\infty, 0)$ for the left, top, and bottom boundaries. A stress-free condition is set for the right boundary. The boundary conditions on the cylinders are updated each time step to simulate their rotation.

To mimic a multifrequency flow, the two rear cylinders are controlled with a periodic signal but with different frequencies. The peripheral speed of the top and bottom cylinders is set to $b_T = \cos(2\pi f_{c1}t)$ and $b_B = \cos(2\pi f_{c2}t)$, respectively. The frequencies are set to $f_{c1} = \sqrt{\pi}f_0$ and $f_{c2} = \pi f_0$, and the corresponding periods are $T_{c1} \approx 6.41$ and $T_{c2} \approx 3.62$. The π and $\sqrt{\pi}$ coefficients are chosen so that the local dynamics of the flow are incommensurable with the natural vortex shedding. For this study, 10000 snapshots in the post-transient regime are sampled at $\Delta t = 0.1$. This corresponds to more than 80 periods of the unforced flow. Figure 2b shows the vorticity field for one snapshot.

3.2 Spatial manifold

For spatial partitioning of the flow field, points on the unstructured grid are used directly. This allows better separation of the subdomains in regions where the mesh is refined. The spatial manifold is built following the methodology described in §2.2. $k = 10$ neighbors are considered during the ISOMAP step to build the spatial manifold. Figure 3 describes the obtained manifold, where the residual variance presents one minimum for four subdomains. Hence, only the first four manifold coordinates are considered. The spatial manifold displays a butterfly-type shape, see figure 3 (c). Interestingly, the wings are carried on the external side by points on the rear cylinders. The points on the front cylinder form the skeleton of both antennas as they connect in the center of the manifold.

Figure 4 gives an interpretation of the manifold coordinates. For the interpretation of γ_1 , five evenly-spaced points along γ_1 are sampled. First, the points with minimum and maximum γ_1 are selected. The remaining points are the manifold points that are the closest to a linear interpolation between the two extremal ones. The Power Spectral Density (PSD) of each point is displayed in figure 4(a). The results suggest that γ_1 is related to the spectral content of the local time series. More precisely, γ_1 describes a continuous transition from f_{c1} (low γ_1 values) to f_{c2} (high γ_1 values). A similar analysis carried out on the second manifold coordinate suggests that γ_2 is related to the power level of the natural frequency f_0 . For the third manifold coordinate, the scalar plot —figure 4(c)— suggested that γ_3 is related to the mean vorticity of the points. Finally, figure 4 shows a piece-wise linear relationship between the root mean square value of the vorticity and γ_4 . The fourth manifold coordinate seems to describe a non-standard quantity whose interpretation needs further investigation.

3.3 Local cluster-based models

Figure 5 gives an exploded view of the fluidic pinball and the nine subdomains. The number of temporal clusters (subsequences) for the cluster-based network models is obtained via the TLF method detailed in §2.2. The method gives two subsequences for subdomains 1, 2, 4, 5, and 6, five subsequences for subdomains 7 and 9, eight for subdomain 3, and nine for subdomain 8. An analysis of the autocorrelation of the original data and the prediction data shows an excellent overlap for all cases except subdomains 3 and 8 (not shown here). The dominant period T_i of the coherent structures is obtained through the first zero of the autocorrelation function. The periods are summarized in Table 1.

Three groups of subdomains stand out. The first group includes subdomains 1, 4, and 6 (dashed boxes). The period associated with these subdomains corresponds to the forcing period of the top cylinder ($T_{c1} = 6.41$). Although these subdomains share similar dynamics, the spatial clustering separates them into distinct clusters. This is explained by

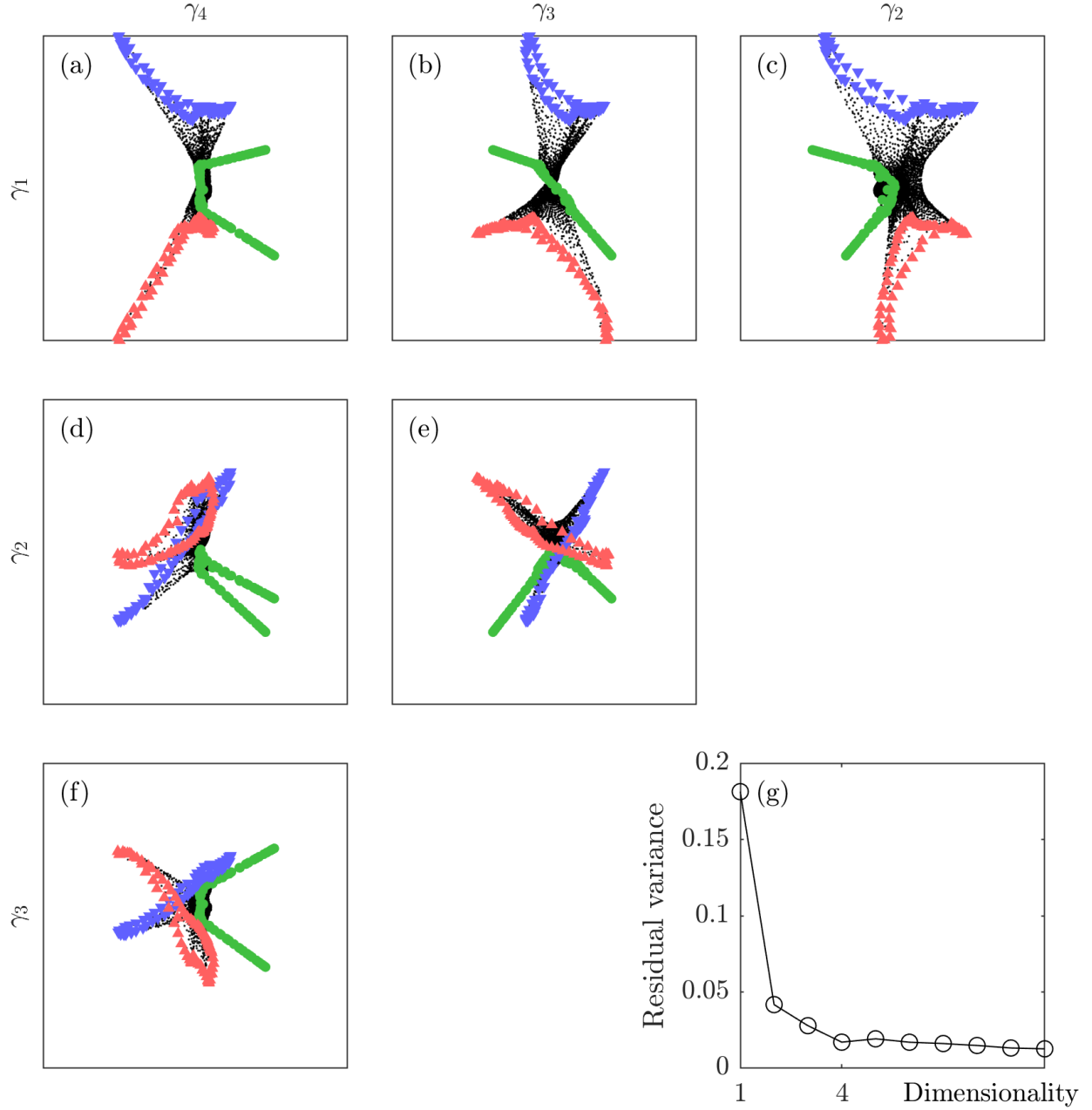


Figure 3: Spatial manifold for the fluidic pinball. (a-f) Projection of the manifold on the first four manifold coordinates. The points on the cylinders are indicated with \bullet , \blacktriangledown , and \blacktriangle for the front, bottom, and top cylinders, respectively. The remaining points are indicated with black dots. (g) Residual variance as a function of the dimensionality of the manifold.

Cluster #	1	2	3	4	5	6	7	8	9
Original data	6.34	3.64	4.19	6.39	3.62	6.42	3.79	8.64	11.65
CNM prediction	6.41	3.62	4.36	6.41	3.62	6.41	3.62	9.13	11.96

Table 1: Dominant period for each subdomain of the fluidic pinball obtained via the first zero of the autocorrelation function.

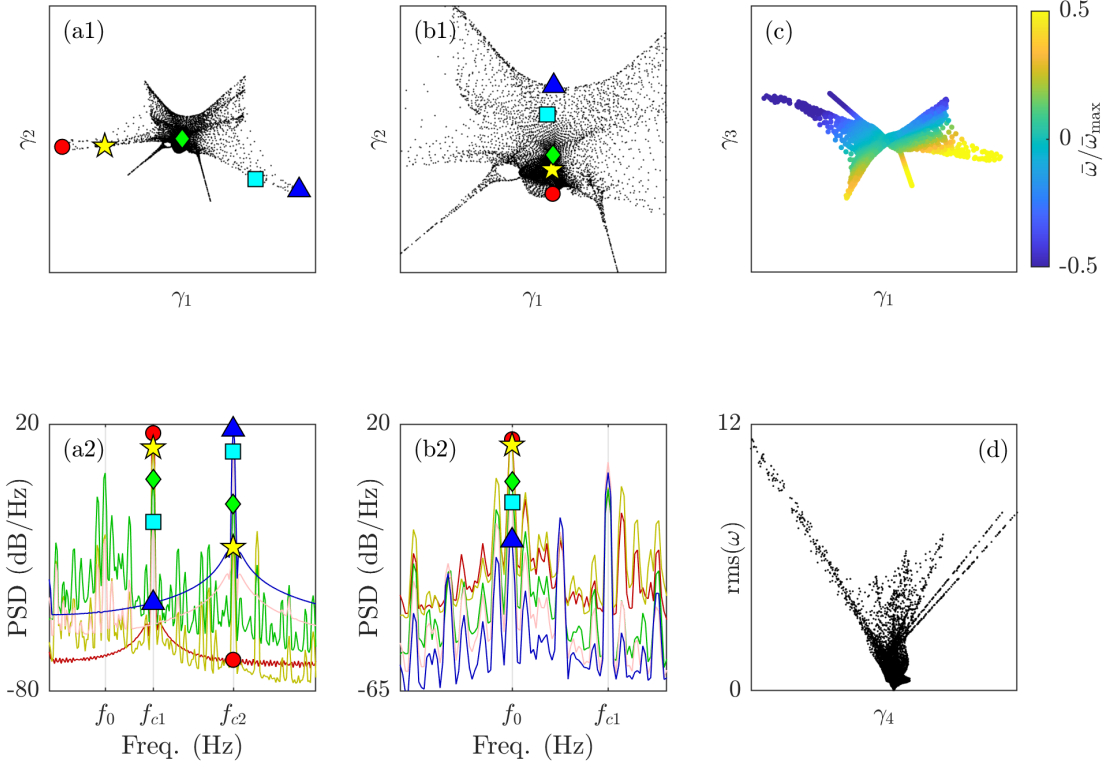


Figure 4: Interpretation of the spatial manifold coordinates γ_i for the fluidic pinball. (a1) Selected points on the spatial manifold “evenly” sampled from maximum to minimum γ_1 . (a2) PSD of the v -velocity of the points sampled in (a1). The symbols indicate the corresponding power levels for f_{c1} and f_{c2} . (b) Similar to (a) for points sampled along γ_2 . (c) Data points colored by the mean vorticity. (d) Data points projected on the plane $\gamma_4 - \text{rms}(\omega)$.

the average vorticity of these subdomains. Indeed, we have seen that the third spatial feature γ_3 is correlated with the average vorticity, and the values for subdomains 1, 4, and 6 are -5.31 , 1.48 , and -6.28 , respectively. Subdomains 2, 4, and 7 form the second group (dotted-line boxes). The periods computed from the autocorrelation function correspond to the forcing period of the bottom cylinder, T_{c2} . Similar to the first group, the distinction between the clusters is explained by the average vorticity level. The last group (solid-line box) is the subdomain 9 alone. This subdomain describes the far-field dynamics, whose dominant period is slightly greater than that of the unforced flow. Subdomains 3 and 8 (dot-dashed-line box) display complex networks whose dominant period is not related to f_0 , f_{c1} , or f_{c2} . They are further interpreted below.

Figure 6 shows the centroids for the 5-subsequence subdomains. For subdomain 7, the velocity fields show that the clusters are related to the rotation of the bottom cylinder. The velocity changes sign between windward and leeward of the bottom cylinder, but keeps similar intensity. Note that the velocity field indicates a displacement of the fluid in the opposite direction to the rotation of the cylinder. For example, for subsequence 1, the bottom cylinder rotates clockwise on average, but the fluctuation of velocity is negative on the windward side and positive on the leeward side of the cylinder. This is due to the phase delay between the generation of vorticity by the cylinder rotation and its propagation through viscous diffusion. This description fits subsequences 1, 2, and 5. For subsequences 3 and 4, the velocity field corresponds to the rotation direction. Those subsequences may correspond to phases of the flow where the cylinder rotation is about to change sign or has just done so.

On the other hand, subdomain 9 represents the far-field where the dynamics are driven by the global vortex shedding. The centroids are averaged vorticity fields in a subsequence. The sequence of snapshots describes the shedding of a vortex and its advection downstream. Note that the averaged flow does not resolve the small structures in the vorticity branches.

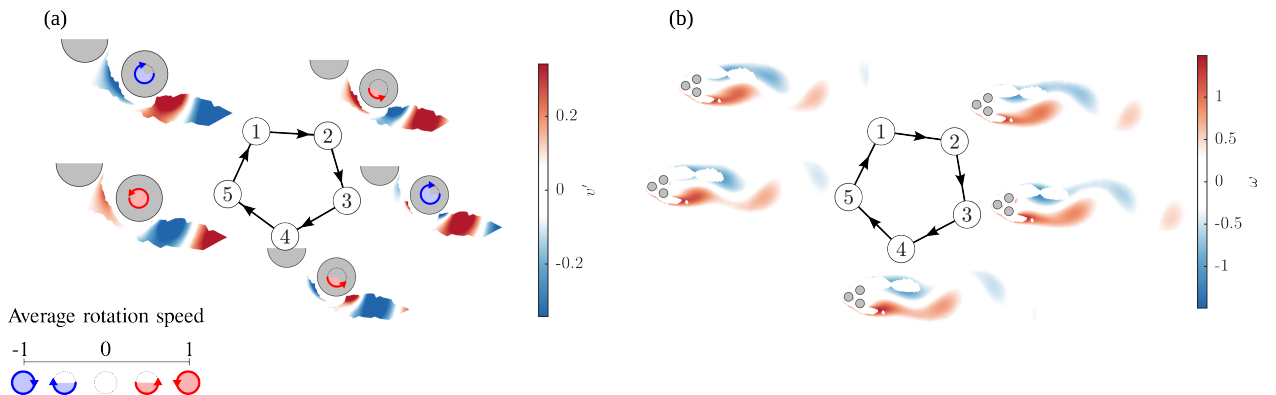
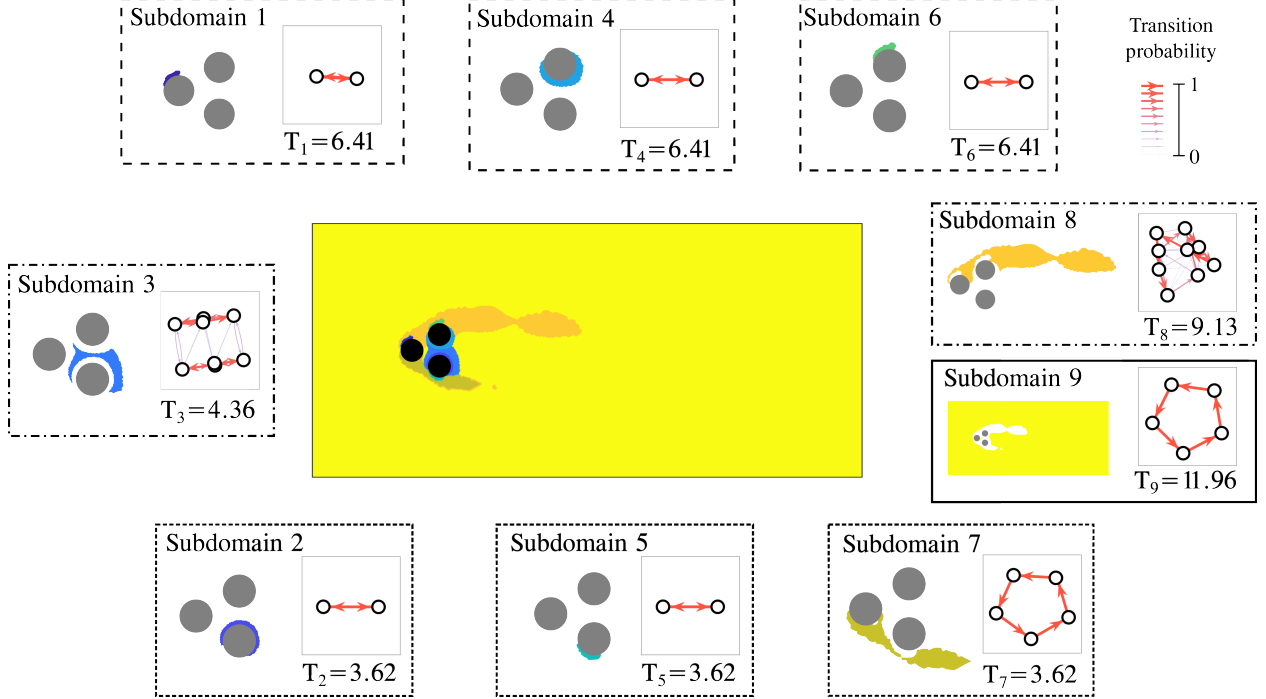


Figure 6: Description of 5-subsequence subdomains. Depiction of the centroids, transition and snapshots for (a) subdomain 7 and (b) subdomain 9. The circular arrows indicate the average rotation speed of the cylinder for each subsequence. A full circle corresponds to a peripheral speed of 1 D per convective time unit.

Figure 7 details the cluster-based model of subdomain 3. The transition probability matrix unveils two dominant cycles in the network model: $\mathcal{S}_1 \rightarrow \mathcal{S}_2 \rightarrow \mathcal{S}_3 \rightarrow \mathcal{S}_4$ and $\mathcal{S}_5 \rightarrow \mathcal{S}_6 \rightarrow \mathcal{S}_7 \rightarrow \mathcal{S}_8$. The remaining low probability transitions indicate switches from one cycle to another. A closer inspection of the velocity fields and the rotation speed shows that the two cycles represent the same behavior with opposite signs. Cycles \mathcal{C}_1 and \mathcal{C}_2 describe the clockwise and counterclockwise rotation of the top cylinder, respectively. The four subsequences in each cycle describe the rotation of the bottom cylinder. Two subsequences describe the clockwise rotation (\mathcal{S}_2 and \mathcal{S}_3 for \mathcal{C}_1 and \mathcal{S}_7 and \mathcal{S}_8 for \mathcal{C}_2) and the other two, the counterclockwise rotation. The transition time matrix shows that \mathcal{C}_1 and \mathcal{C}_2 have different periods, 3.17 and 3.11, respectively. This difference is explained by the incommensurability of f_{c1} and f_{c2} , i.e., T_1 and T_2 do not have a common measure.

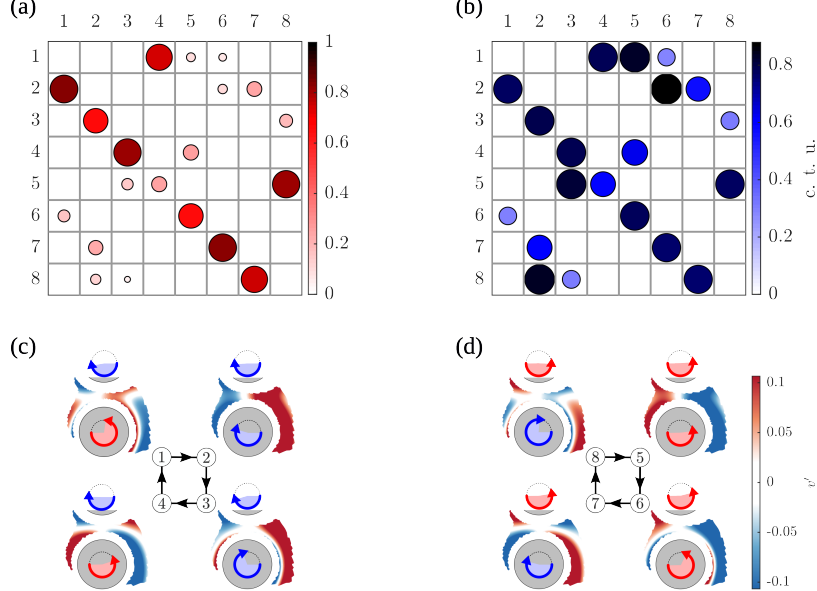


Figure 7: Description of subdomain 3. (a) Transition probability matrix; (b) Transition time matrix. c. t. u. stands for convective time units. The transition probability matrix suggests the dynamics include two cyclic trajectories ($\mathcal{S}_1 \rightarrow \mathcal{S}_2 \rightarrow \mathcal{S}_3 \rightarrow \mathcal{S}_4$ and $\mathcal{S}_8 \rightarrow \mathcal{S}_5 \rightarrow \mathcal{S}_6 \rightarrow \mathcal{S}_7$). The arrows denote the average rotation speed of each subsequence, as in Figure 6.

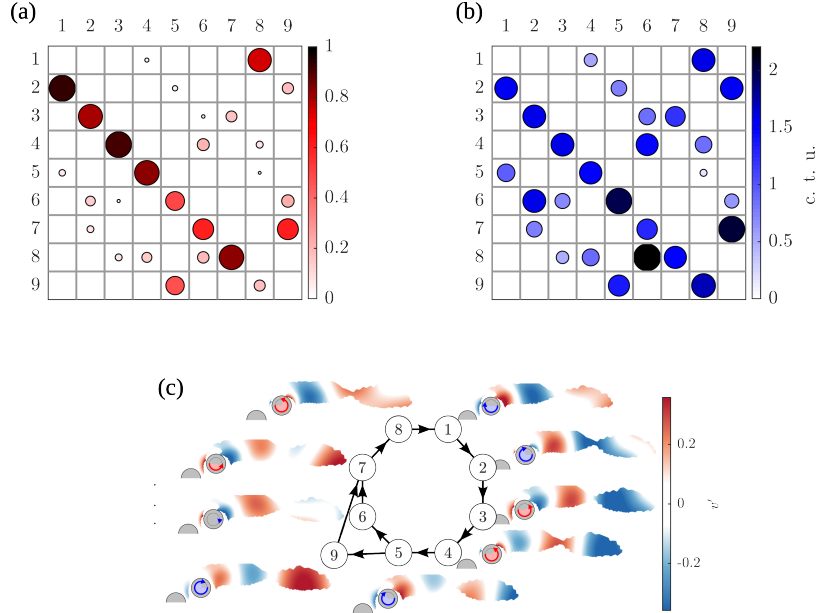


Figure 8: Similar to Figure 7 but for subdomain 8. (c) shows the main cycle, obtained by following the largest probability transitions.

Figure 8 details the dynamics of subdomain 8. Similarly to subdomain 3, each phase of the control is represented by two subsequences, corresponding to the increase and decrease of the actuation level. Two cycles can be inferred from the transition probability matrix: $\mathcal{S}_1 \rightarrow \mathcal{S}_2 \rightarrow \mathcal{S}_3 \rightarrow \mathcal{S}_4 \rightarrow \mathcal{S}_5 \rightarrow \mathcal{S}_6 \rightarrow \mathcal{S}_7 \rightarrow \mathcal{S}_8$, and $\mathcal{S}_1 \rightarrow \mathcal{S}_2 \rightarrow \mathcal{S}_3 \rightarrow \mathcal{S}_4 \rightarrow \mathcal{S}_5 \rightarrow \mathcal{S}_9 \rightarrow \mathcal{S}_7 \rightarrow \mathcal{S}_8$. They display slightly different periods, 12.70 and 12.84, respectively, suggesting two different dynamics are at play. The second one is related to the forcing for two reasons. First, its period corresponds approximately to $2T_{c1}$. Second, this cycle includes subsequence 9 with a large actuation level. The first cycle may

result from an interaction between the forcing and the far-field dynamics. The subsequence 5 is the key to the change of dynamics.

As for subdomains 1, 2, 4, 5, and 6, they all describe a periodic behavior on the surface of the cylinders. They are further detailed in Appendix A.

The proposed methodology isolates regions of the flow, revealing complex local dynamics that cannot be obtained with a global approach. Indeed, a global network model of the flow gives a single deterministic cycle with period 12.02, see Appendix B.

4 Local interpretation of an experimental jet flow

In this section, the method is validated with an experimental dataset of planar PIV of a water jet flow. The objective is to aid the global modeling of the flow by identifying regions where the dynamics are simple and interpretable.

4.1 Configuration and data description

Planar PIV experiments of a water jet flow (see figure 9) are conducted in the water tank facility of the Experimental Aerodynamics and Propulsion lab at Universidad Carlos III de Madrid. The tank has full optical access with dimensions $80 \times 60 \times 40 \text{ cm}^3$. The jet has a nozzle with an exit diameter of $D = 0.03 \text{ m}$ and is operated at a bulk velocity of $U_b \approx 0.11 \text{ m/s}$. The corresponding Reynolds number based on U_b and D is $Re \approx 3300$, corresponding to a transitional jet flow [Bogey and Bailly, 2006, Fellouah et al., 2009, Mi et al., 2013]. The flow is seeded with polyamide particles of $54 \text{ }\mu\text{m}$ diameter and is illuminated at the midplane of the nozzle exit with a 5W *LaserTree LT-40W-AA* pulse-width modulated laser. The laser beam is shaped into a thin plane of approximately 1mm thickness using a spherical converging lens and two cylindrical diverging lenses, as depicted in figure 9(a). For further insights into the experimental setup, the reader is referred to Franceschelli et al. [2025]. Flow snapshots are acquired with an *Andor Zyla sCMOS camera* with a sensor of 5.5 megapixels ($2160 \times 2560 \text{ px}$, with a pixel size of $6.5 \text{ }\mu\text{m}$). The field of view covers a domain of $8D \times 2.6D$ spanning from the nozzle exit and centered vertically with the centerline of the jet such that $x/D \in [0, 8]$ and $y/D \in [-1.3, 1.3]$, nondimensionalized with the jet diameter. The Cartesian coordinate x points in the direction of the jet flow, while y is orthogonal to x , pointing in the upwards in the vertical direction. The velocity fields are correspondingly nondimensionalized with the bulk velocity. The field of view is delimited by a red dashed rectangle in figure 9(b). Finally, figure 9(c) shows the nondimensional vorticity field at a given instant. The small upward deflection is due to asymmetry in the top-bottom boundary conditions.

The dataset consists of a sequence of 60000 time-resolved snapshots captured with a time step of $\Delta t = 0.011 \text{ s}$. The PIV images are processed with a custom-made multi-frame approach, based on sliding cross-correlation of a 5-frame stencil [Scarano and Moore, 2010]. The processing consists of three-pass cross-correlation analysis with the final interrogation windows of $32 \times 32 \text{ px}$ with 75% overlap. To remove measurement noise, the velocity fields are smoothed with a second-order polynomial Savitzky-Golay filter with a 5×5 kernel in space, and 5 snapshots in time. For the demonstration of the methodology, 5000 snapshots, subsampled by a factor of 4, are considered. This choice alleviates the computational load by obtaining converged statistics with a reduced number of snapshots.

The jet flow at $Re \approx 3300$ corresponds to a transitional jet that is characterized by the presence of localized dynamics in the flow due to the generation and breakdown of ring vortices and turbulent mixing [Fellouah et al., 2009, Ball et al., 2012]. This compound picture of the flow motivates our choice of the jet flow for the experimental validation of the proposed method.

4.2 Spatial manifold and clustering results

To identify regions with similar features and dynamics, the spatial manifold of the vorticity fields is computed with ISOMAP according to the methodology presented in §2. The first three manifold coordinates are selected for the low-dimensional representation as they minimize the residual variance computed according to Equation 3. The resulting three-dimensional manifold resembles a space coffee cup-like shape and is depicted in figure 10.

To interpret the manifold coordinates, four points are sampled along each direction in the manifold space (see figure 10(b-d), and the corresponding PSD of the v velocity component is computed. Interestingly, γ_1 and γ_2 seem to be correlated with the streamwise and spanwise direction of the flow. This is partially supported by the distribution of clusters (figures 10e and 11), e.g., subdomains 6 (yellow) and 1 (darkest green) are located at low and large values of γ_1 , respectively. The PSD of the points distributed along γ_1 shows clearly two different dominant frequencies, meaning that there dynamics change across this regime. Additionally, it can be noted that the intensity of the PSD depends directly on the value of γ_1 , thus increasing for increasing values of γ_1 . As for γ_2 , the points sampled far

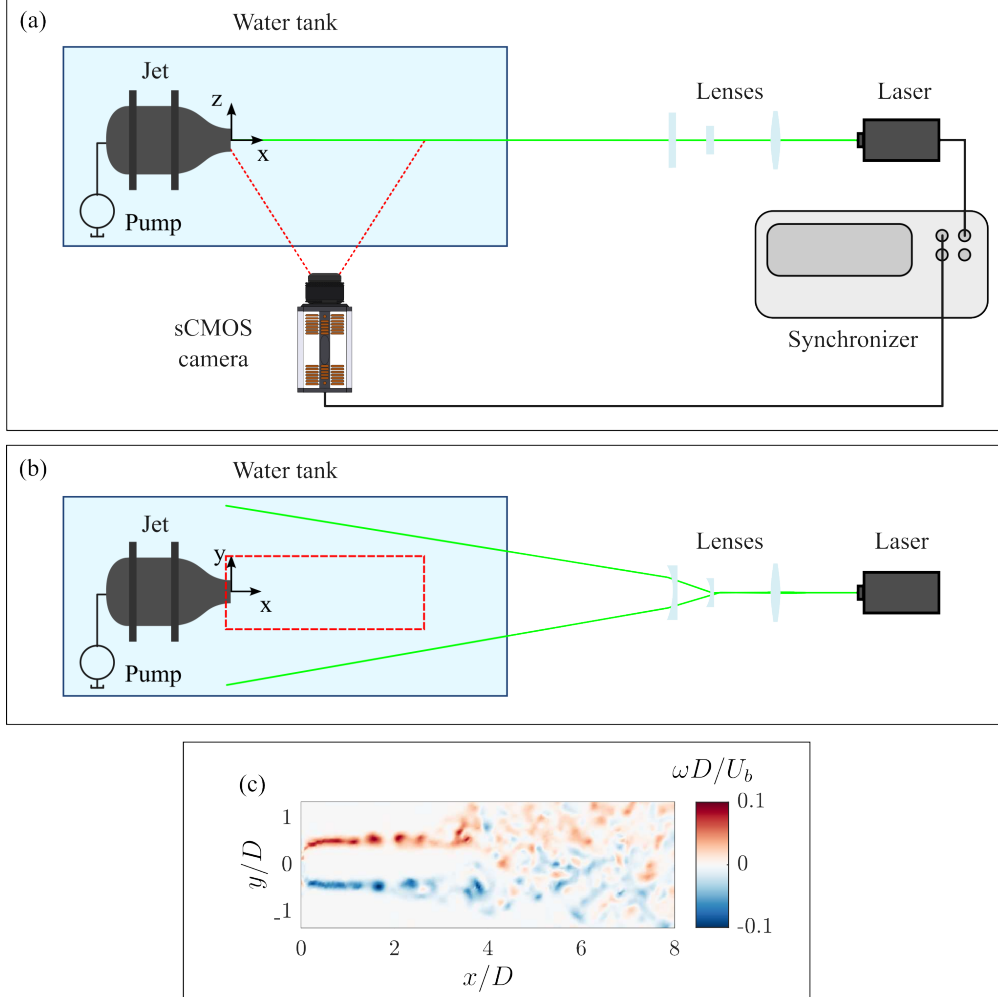


Figure 9: Schematics of the planar PIV setup for the jet flow experiment in water. (a) Top view and (b) front view. The laser plane, opened with the optical path, is depicted in green, and the field of view of the PIV camera in red. Figure adapted from Franceschelli et al. [2025], under license CC BY 4.0. (c) Vorticity field of a sample snapshot.

from $\gamma_2 = 0$ seem to include a peak at $St = 0.30$ ($f \approx 1.1$ Hz) that is mitigated as γ_2 decreases in absolute value. Additionally, points that are clustered together in the same subdomain retrieve similar dominant frequencies, as can be noticed in figure 10(d1). On the other hand, γ_3 correlates well with the PSD intensity. Namely, moving towards a more negative γ_3 results in a higher intensity of the PSD. Lastly, in figure 10(e), we note a symmetry along the γ_2 direction equivalent to the symmetry with respect to the x axis. Close to the symmetry plane, the dominant frequencies are similar, while moving away, the dominant frequencies show similar intensities. The symmetry of the configuration explains the symmetry of the spatial manifold along the γ_2 axis. The deviation from perfect symmetry may be explained by the deflection of the jet towards the free surface of the water tank.

The spatial manifold is clustered into 6 subdomains following the TLF criterion. The corresponding clustered domain is depicted in figure 11, where the subdomains are ordered according to their total kinetic energy. In Appendix C.1, the effect of a larger and smaller number of subdomains is assessed. The comparison between the clustered manifold and the clustered domain suggests that γ_1 and γ_2 are correlated with the physical coordinates of space. This represents an interesting feature of the method, since it is capable of identifying a spatial distribution with clear interpretability in the physical space, without introducing explicitly any information about the real coordinates.

Furthermore, it is interesting to note that, similar to the pinball, the largest domain (subdomain 6) is condensed into a small, clustered area in the manifold. A reason behind this might be the clear dominance of a dynamics, which in this region corresponds mainly to the shear layer where the generated vortices roll up and then pair up [Ball et al., 2012].

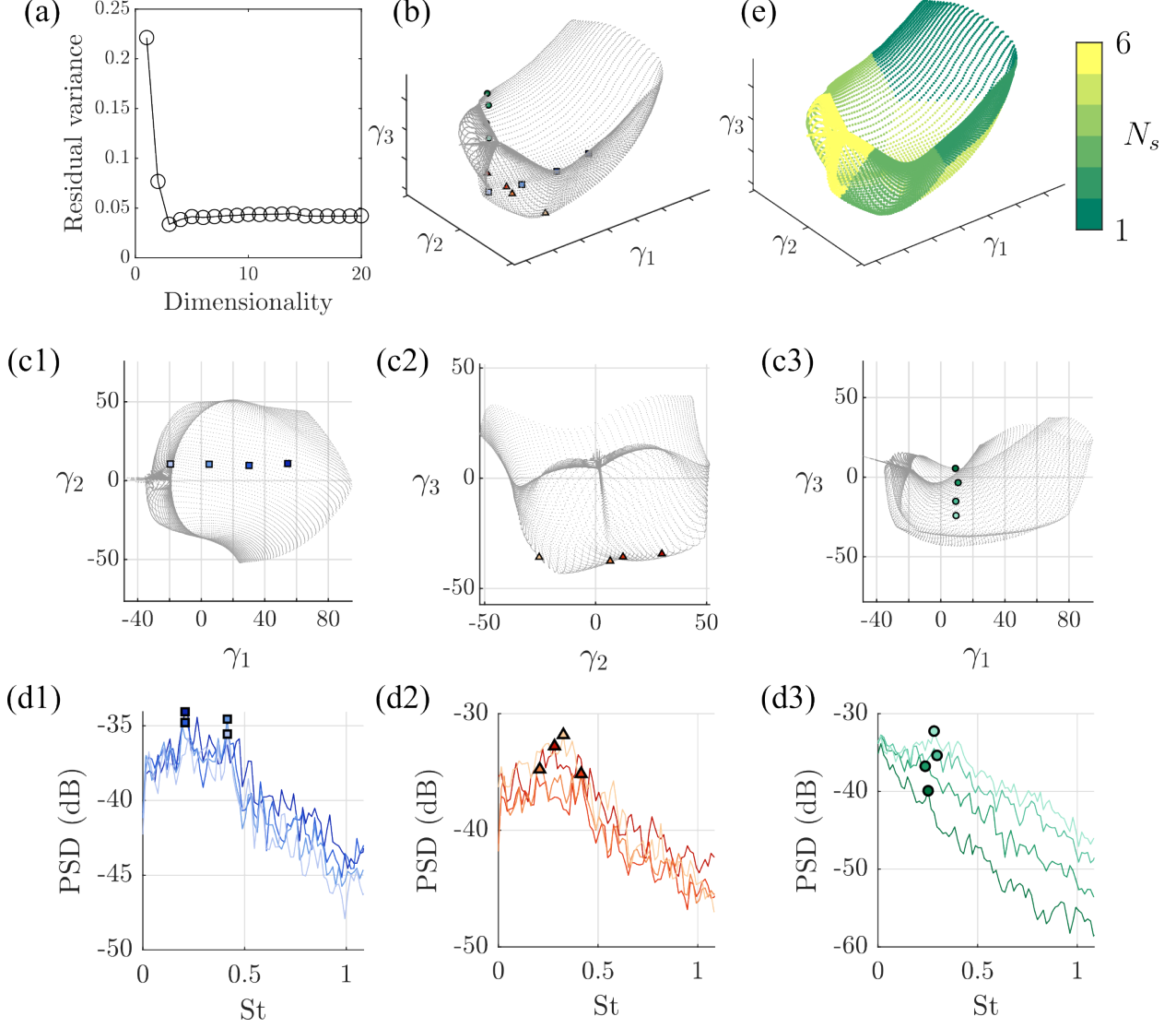


Figure 10: Spatial manifold of the jet flow data. (a) Residual variance versus the dimensionality of the spatial reconstruction. (b) Three-dimensional spatial manifold. Blue colored squares mark points with γ_2 and γ_3 approximately constant ($\gamma_2 \approx 10$ and $\gamma_3 \approx -35$). Orange colored triangles mark points with γ_1 and γ_3 approximately constant ($\gamma_1 \approx -5$ and $\gamma_3 \approx -36$). Green colored circles mark points with γ_1 and γ_2 approximately constant ($\gamma_1 \approx 10$ and $\gamma_2 \approx 49$). (c1-3) 2D views of the spatial manifolds with sampling points. (d1-3) PSD of the v -velocity at the sampled points. (e) Clustered manifold with 6 subdomains.

On the other hand, in regions where complexity increases due to mixing and turbulence, the corresponding manifold areas are seen to be larger as the dynamics are spectrally broadband.

4.3 Local cluster-based modeling

The analysis of the dynamics in each of the spatial domains is done through cluster-based modeling. Figure 11 shows an exploded view of the jet flow into the six subdomains. Then, for each subdomain, the cluster-based models are extracted, with the corresponding number of temporal clusters selected according to the two-line fit criteria. For each of these cases, the snapshots are reconstructed by interpolating between the subsequence centroids. The autocorrelation between the reconstructed snapshots and the original ones is used to assess whether the local models are representative of the dynamics. Results show that only Subdomains 5 and 6 present similar periods (first zero crossing point), thus

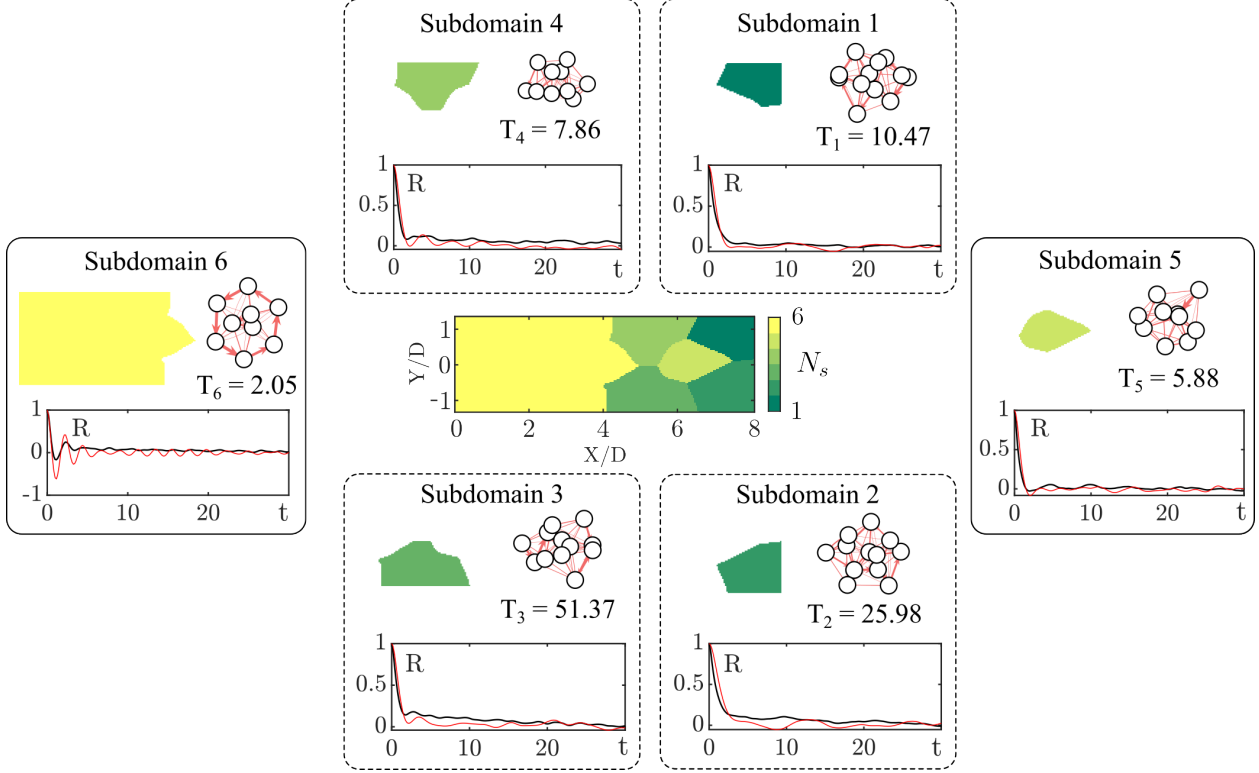


Figure 11: Local interpretation of the experimental water jet flow. The flow is partitioned into 6 subdomains. Each subdomain is accompanied by the cluster-based network model built on the masked snapshots and the autocorrelation functions of the original snapshots and the reconstructed snapshots as a function of the time nondimensionalized with the convective time. The dots correspond to the centroids in the subsequences projected on the first two POD modes. The times T_i correspond to the first zero of the autocorrelation function of the reconstructions. The autocorrelation functions are depicted for the predicted data (red line) and the original data (black line).

Cluster #	1	2	3	4	5	6
Original data	72.14	115.03	130.48	149.94	5.91	2.67
CNM prediction	10.47	25.98	51.37	7.86	5.88	2.05

Table 2: Dominant nondimensional period for each subdomain of the jet flow obtained via the first zero of the autocorrelation function.

the analysis and discussion of the results are only assessed for these two subdomains. All periods are summarized in Table 2.

In the other subdomains, high turbulent mixing with three-dimensional effects is observed due to chaotic behavior and turbulent dynamics, rendering the modeling of the dynamics impractical.

Finally, figure 12 presents the results of the local Markov models, showing the transition probability matrix with the corresponding transition time matrix. For subdomain 6, the cluster model indicates a switch between two phases, that can be identified from the transition probability matrix ($\mathcal{S}_1 \rightarrow \mathcal{S}_2 \rightarrow \mathcal{S}_3 \rightarrow \mathcal{S}_4 \rightarrow \mathcal{S}_5 \rightarrow \mathcal{S}_6$ and $\mathcal{S}_7 \rightarrow \mathcal{S}_8 \rightarrow \mathcal{S}_9$) with periods $T_{6,1} = 2.29$ and $T_{6,2} = 1.84$, respectively. The first phase is characterized by two large vortices, while the second displays three small vortices. Both cycles describe the dynamics of the vortex shedding mechanism, with the difference that the first one captures the dynamics post-vortex pairing, similarly to the work of Kaiser et al. [2014], where the authors identify two cycles in a mixing layer: one related to the Kelvin-Helmholtz instability and the other to a vortex pairing. These dynamics are confirmed with a refined model based on 20 clusters, see Appendix C. This high-resolution model identifies a centroid where two vortices merge that serves as a transition between the two cycles. However, this analysis is presented for the sake of interpretation and not for the identification of limit cycles. Increasing the number of clusters highly reduces the number of snapshots per cluster, thus increasing the variability of results

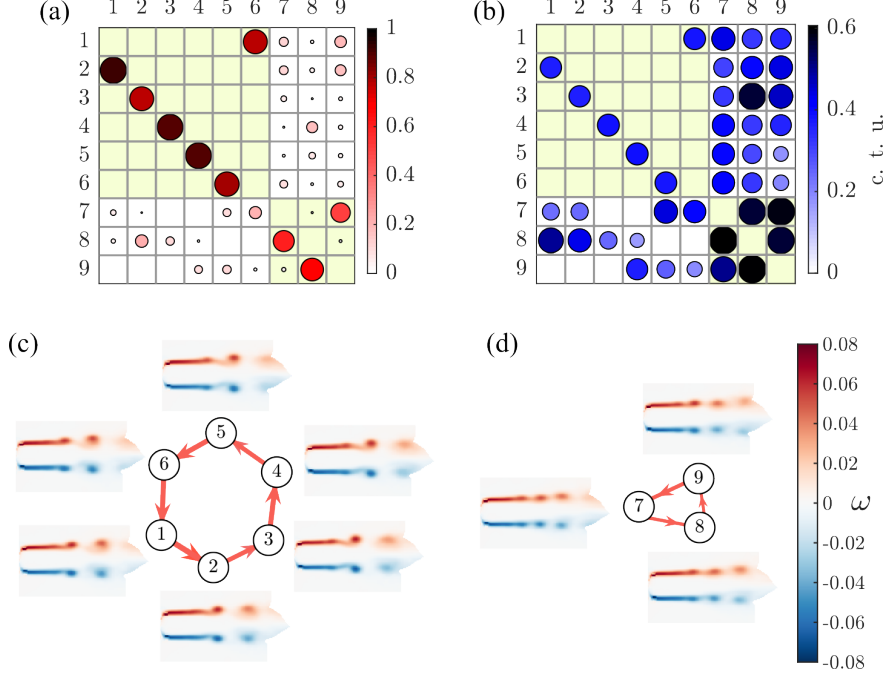


Figure 12: Description of subdomain 6. a) Transition probability matrix. b) Transition time matrix. The transition probability matrix suggests that dynamics include two periodic trajectories ($S_1 \rightarrow S_2 \rightarrow S_4 \rightarrow S_5 \rightarrow S_6$ and $S_7 \rightarrow S_8 \rightarrow S_9$). The corresponding nondimensional vorticity snapshots of the centroids and the subnetworks are displayed in c) and d). Limit cycle 1 has period $T_{6,1} = 2.29$ and cycle 2 of period $T_{6,2} = 1.84$.

despite augmenting the number of replicates in the k -means algorithm. The transition between both phases is between S_2 and S_7 in the low-resolution model.

Moreover, the difference in frequency might be induced by instabilities of the flow coming from recirculation, asymmetry due to the open tank, non-zero pressure gradient, or three-dimensional effects, which cause the vortex shedding to trigger earlier. However, such a difference only comprises a 20% change in the period and corresponding wavelength, which is compared between the vorticity fields of the centroids of S_5 and S_8 . These are selected to be the instant when the first vortex is fully detached. The bulk velocity for both cycles remains unchanged. Evaluating the probability of being in each of the cycles, it is observed that there is the same probability for both cycles, where a regular transition between cycles is observed in a quasi-periodic manner with a period equal to T_6 .

The results of subdomain 5 are represented in figure 13, where a total of 10 clusters have been identified. Different from before, no dominant cycles are identified, but instead, many interconnected cycles can be observed. In this subdomain, flow oscillates in a switching pattern, as it can be seen in the vorticity fields of the corresponding centroids (see figure 13(c)). This waving behaviour is generated by the collision of vortices in the centreline and the three-dimensional interaction of the flow. The result is an oscillating pattern that repeats in time but can follow different paths, i.e., different cycles. It is important to note that due to the high variability of the cycles and the transitions, the k -means clustering was performed with an increased number of replicates, of the order of a thousand, in order to ensure convergence in the cluster transitions.

In summary, the present methodology identifies local dynamics that are not identified with a global approach. The global cluster-based analysis does not properly identify the separate dynamics observed in subdomain 6 nor the oscillation of subdomain 5. The dynamics are mixed together without retrieving a clear separation between them, see Appendix D.

5 Discussion and conclusions

This paper introduces ST-CNM, a method to identify local dynamics that are not captured by global methods. The starting point is a space and time-resolved snapshot dataset. The method first consists of the decomposition of the flow domain with an unsupervised method applied directly on the data points. The key enabler is the definition of

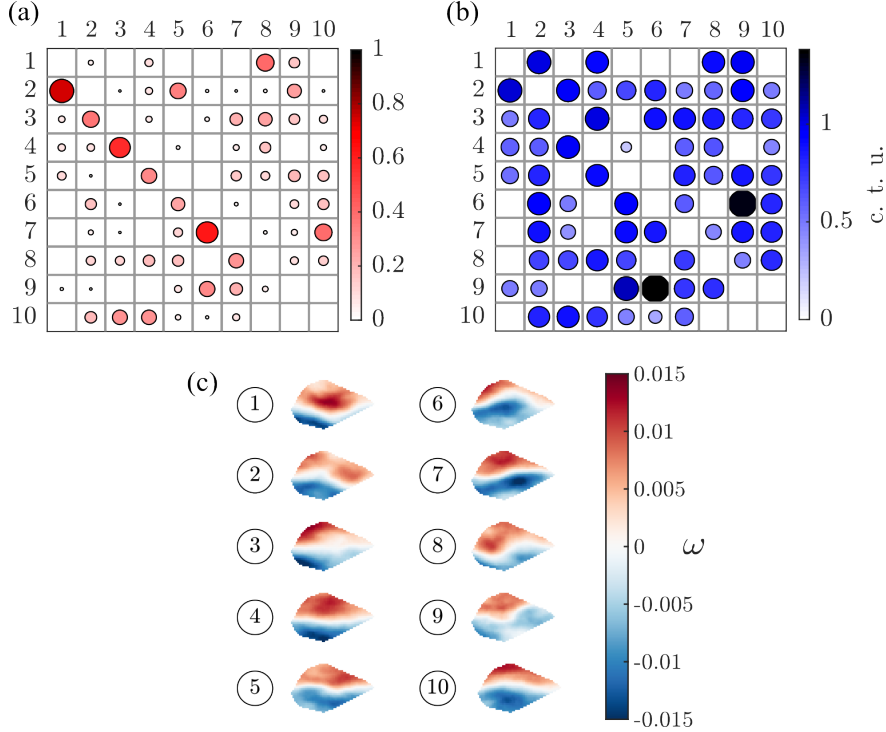


Figure 13: Description of subdomain 5. (a) Transition probability matrix. (b) Transition time matrix c. t. u. stands for convective time units. Transition probability matrix suggests the dynamics include a periodic trajectory ($S_2 \rightarrow S_3 \rightarrow S_4 \rightarrow S_5 \rightarrow S_6 \rightarrow S_7$). The period of the cycle is $T = 6.07$. (c) Nondimensional vorticity snapshots of the cluster centroids.

a low-dimensional representation of the flow domain that separates the regions based on the local dynamics. This low-dimensional space, termed spatial manifold, is obtained via a nonlinear decomposition of the vorticity field with ISOMAP. Then, each of the corresponding subdomains is clustered in time, according to the cluster-based network model methodology, to build local Markov models. The number of spatial and temporal clusters is decided by the TLF method, making the process fully automated without the need for any meta-parameter tuning. The method is demonstrated on two flows: a numerical simulation of the fluidic pinball under control and the PIV data of an experimental jet flow at $Re \approx 3300$.

For the fluidic pinball, the flow is forced by a periodic rotation of the rear cylinders at incommensurable frequencies. ISOMAP identifies a four-dimensional space that represents the spatial distribution of the dynamics. Interestingly, the first three spatial manifold coordinates are related to the main local frequency, the intensity of the vortex shedding frequency, and the average local vorticity. The fourth manifold coordinate represents a nonlinear feature. The k -means algorithm applied to the manifold coordinates separates the domain into 9 subdomains and identifies the global vortex shedding and local periodic behaviors related to the forcing that are not captured with a global approach. Intriguingly, the periodic oscillation of the top cylinder is also perceived upstream, on the surface of the front cylinder. Although the small regions near the cylinders share the same periodic behavior, they are separated due to their average vorticity level. Finally, the method identifies two regions with complex dynamics: (1) the region between the two rear cylinders is under the influence of two incommensurable rotations, and (2) the wake of the top cylinder that experiences a nonlinear interaction with the global vortex shedding. The method suggests that those regions require further modeling effort to accurately represent the local dynamics.

Results of an experimental dataset have been presented for the planar PIV of a transitional jet flow. In this case, ISOMAP identifies a three-dimensional space to represent the dynamics. In this low-dimensional space, the first and second manifold coordinates are closely related to the spatial coordinates, meaning that the model is able to automatically identify a relation with the real geometry of the flow field without any prior information. On the other hand, the third manifold dimension does not present such a strong relationship but shows a change in the power level of the PSD. The partitioning of the domain with k -means retrieves 6 subdomains maintaining the symmetry of the flow. Firstly, a main subdomain is identified where the shear layer, vortex formation, and pairing occur. The corresponding local Markov model is able to identify and separate the dynamics of the vortex shedding phenomena and the vortex

pairing. Downstream of the potential core, a second subdomain is identified where the oscillating dynamics of the flow are identified, and finally, the remaining subdomains are observed to be turbulent with strong mixing. The method is shown to be capable of identifying local dynamics that, otherwise, in a global analysis cannot be directly identified.

Although we propose a method to select the number of clusters, the framework allows a description of the flow at virtually all levels of granularity in time and space. However, the relevance of the description depends on the data resolution. The proposed method constitutes a diagnostic tool to locate regions with complex dynamics that may require additional modeling efforts as opposed to classical projection-based methods or system identification [Brunton et al., 2016a,b, Peherstorfer and Willcox, 2016, Kramer et al., 2024], or those that require monitoring with increased time and space resolution. The automatization of the process is key to include the method in optimization loops such as design and control, to reduce recirculation regions on complex geometries, or to mitigate local fluctuations at frequencies that may induce resonance, to give a few examples. Future work shall focus on deriving the interaction between the subdomains to build a cluster-based global model of the flow that takes into account the local dynamics and the interaction between subdomains. Another potential line of development is the description of nonstationary flows and the time evolution of the subdomains.

6 Acknowledgements

This project has received funding from the European Research Council (ERC) under the European Unions Horizon 2020 research and innovation program (grant agreement No 949085). Views and opinions expressed are, however, those of the authors only and do not necessarily reflect those of the European Union or the European Research Council. Neither the European Union nor the granting authority can be held responsible for them. We appreciate fruitful discussions with L. Franceschelli, L. Marra, M. Raiola, and I. Tirelli.

A Interpretation of the two-cluster models

Figure A.1 shows the snapshots for the subdomains with only two clusters. They all demonstrate a periodic behavior with a pocket of intense vorticity on the surface of the cylinder that moves following the rotation direction. The pocket of vorticity is rather stable for subdomain 1, as it lies on the front cylinder that does not rotate. However, it is still affected by the rotation of the top cylinder. A symmetric pocket of vorticity on the front cylinder is identified for a larger number of subdomains.

B Global CNM of the fluidic pinball under control

Figure B.1 shows the global CNM of the fluidic pinball under periodic control as described in § 3. The optimal number of clusters following the TLF method is 5. The transition probability network reveals a deterministic transition from one cluster to the other. The transition time from one cluster to the other is similar for all clusters and is approximately 2.4 convective time units. The sequence of vorticity snapshots shows that CNM identifies the dynamics of the far-field vortices, i.e., the shedding of large vortices due to the pairing of the vortices shed by the top and bottom cylinders.

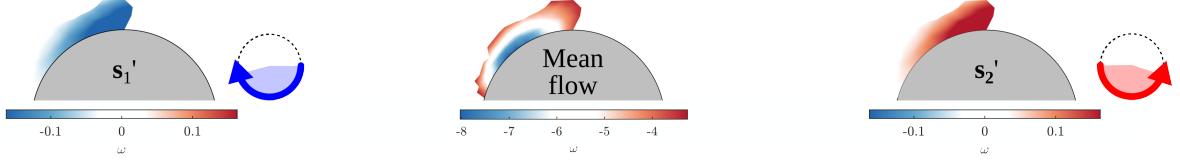
C Local Markov models for jet flow subdomains

C.1 Effect of number of subdomains in spatial clustering of jet flow

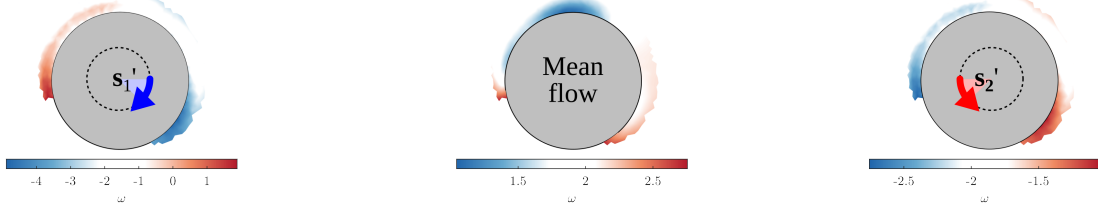
In this section, the effect of the number of subdomains selected for spatial clustering on the spatial distribution of the flow field is assessed. Four different cases have been considered: 3, 11, and 14 subdomains. The corresponding clustered domains are displayed in Figure C.1.

It can be noted that the flow starts clustering into subdomains in regimes where the complexity of the flow highly increases. In the case of the jet flow, this is found downstream of the jet, where high turbulence intensity and mixing take place. Then, when the number of clusters is increased, the flow is clustered further upstream until reaching the optimal clustering with 6 subdomains obtained from the TLF method. With 7 clusters, the results show that it is possible to obtain a cluster isolating the dynamics of the shear layer. Further increasing the number of clusters results in a higher partitioning far downstream in the flow field, but no new clusters are identified.

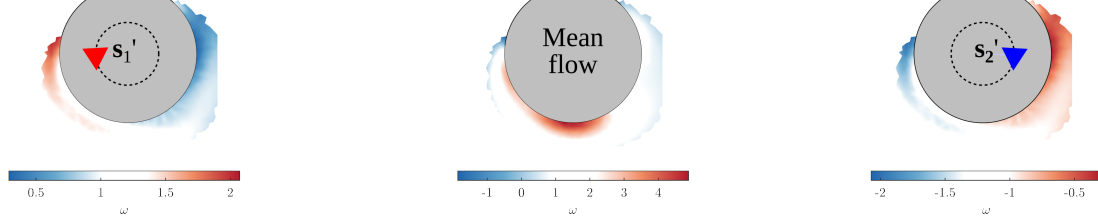
Subdomain 1



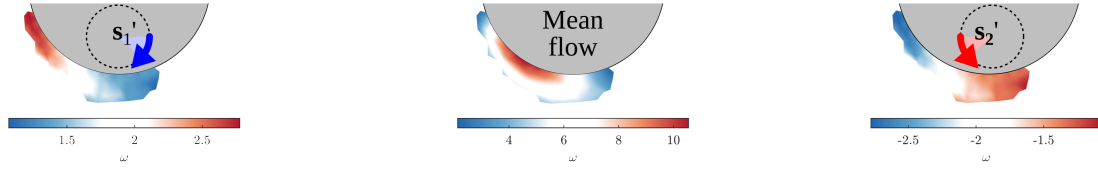
Subdomain 2



Subdomain 4



Subdomain 5



Subdomain 6

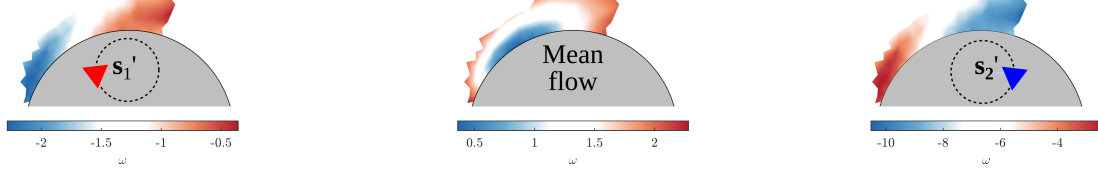


Figure A.1: Description of the network model with only two clusters. For each subdomain, the vorticity of the mean flow is displayed in the central column and the fluctuations in the left and right columns. The first subdomain is located on the surface of the front cylinder that does not rotate. It is under the influence of the top cylinder.

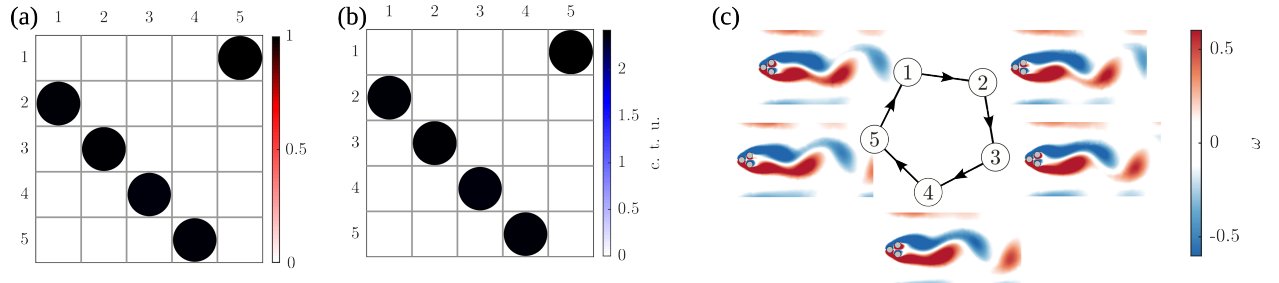


Figure B.1: (a) Transition probability matrix, (b) Transition time matrix and cluster-based model for the fluidic pinball under control as a whole.

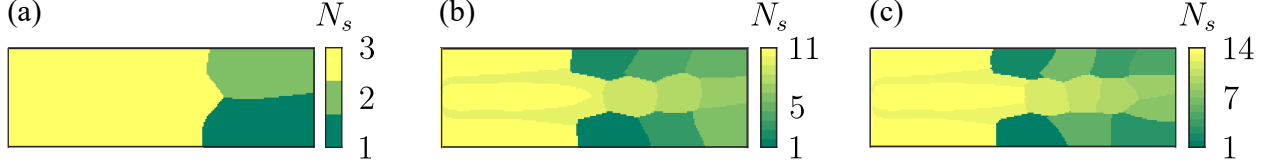
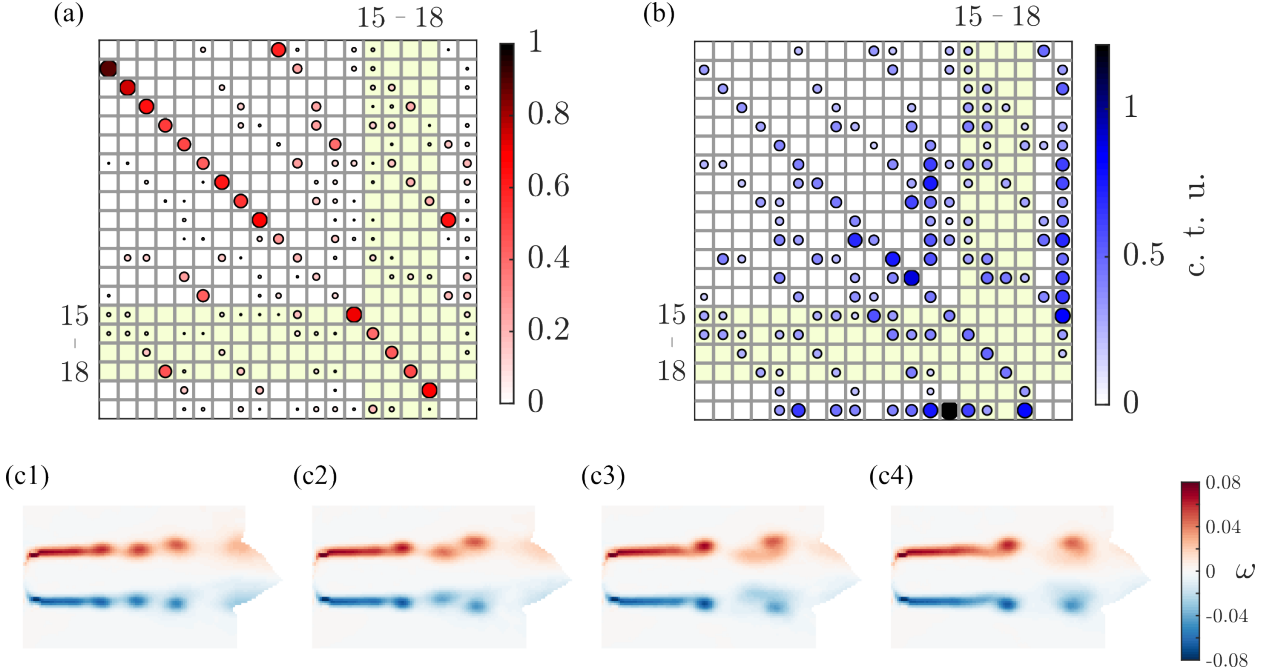


Figure C.1: Spatial partitioning of jet flow with different numbers of subdomains: 3, 11, and 14.

Figure C.2: Description of subdomain 6 with 20 temporal clusters. a) Transition probability matrix. b) Transition time matrix c. t. u. stands for convective time units. c) Nondimensional vorticity snapshots at the centroids of $\mathcal{S}_{15} - \mathcal{S}_{18}$ corresponding to the transition between the vortex shedding and the vortex pairing.

C.2 Analysis of dynamics of jet flow subdomain 6

This appendix presents the analysis of the dynamics in subdomain 6 with a larger number of temporal clusters. To increase the resolution of the dynamics extracted from the local analysis, 20 clusters are used to compute the temporal clustering. Results are presented in Figure C.2. Note that, unlike before, the interpretability of the results is now more complex, as no clear cycles are identified in the transition probability maps. Additionally, when analyzing the transition between centroids, it is observed that the two cycles previously obtained with 9 clusters are now intermixed, indicating a lack of a smooth transition between centroids. This loss of smoothness in the reconstruction of dynamics is due to the small number of samples per cluster, which is not enough to resolve the dynamics within a large number of clusters. However, this extended analysis with more clusters allows identification of the transition snapshots between vortex shedding and the vortex pairing effect. This mechanism is clearly depicted in Figure C.2c) where the vorticity field at the centroids of the transition is represented.

D Global CNM of the jet flow

In this section, the global ST-CNM of the jet flow is discussed as introduced in Section 4. Figure D.1 shows the results of the global analysis of the jet with 9 clusters. A periodic trajectory can be identified between $\mathcal{S}_1 \rightarrow \mathcal{S}_2 \rightarrow \mathcal{S}_3 \rightarrow \mathcal{S}_4$ representing the vortex shedding mechanism that was observed in the local analysis of Subdomain 6. The other centroids do not show a clear trajectory as observed in figure 12, but they represent a transition within the vortex shedding phenomena. Additionally, it is remarkable to mention that no clear dynamics are identified in the region corresponding to Subdomain 5. In the global analysis, the dominant dynamics that can be analyzed are those found

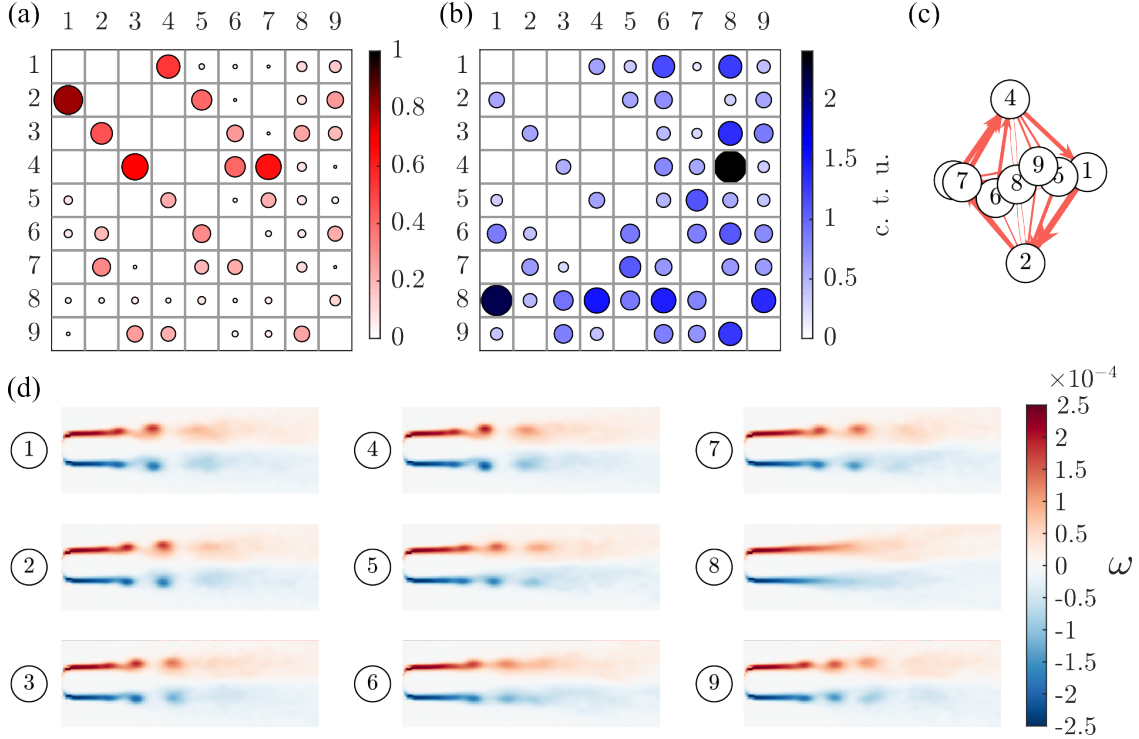


Figure D.1: Jet flow global CNM. (a) Transition probability matrix. (b) Transition time matrix. (c) Cluster centroid map network. (d) Nondimensional vorticity snapshots of the centroids of the clusters.

in Subdomain 6, where only the vortex shedding can be identified. Thus, all the remaining information is grouped together as transition points, as can be seen in the network of figure D.1 c).

References

T. Duriez, S. L. Brunton, and B. R. Noack. *Machine Learning Control — Taming Nonlinear Dynamics and Turbulence*, volume 116 of *Fluid Mechanics and Its Applications*. Springer-Verlag, 2017.

J. Rabault, M. Kuchta, A. Jensen, U. Réglade, and N. Cerardi. Artificial neural networks trained through deep reinforcement learning discover control strategies for active flow control. *J. Fluid Mech.*, 865:281–302, 2019.

S. L. Brunton, B. R. Noack, and P. Koumoutsakos. Machine learning for fluid mechanics. *Ann. Rev. Fluid Mech.*, 52: 477–508, 2020.

J. L. Lumley. The structure of inhomogeneous turbulent flows. In A. M. Yaglom and V. I. Tatarsky, editors, *Atmospheric Turbulence and Radio Wave Propagation*, pages 166–177. Nauka, Moscow, 1967.

Q. L. Li-Hu, P. García-Caspueñas, A. Ianiro, and S. Discetti. Model-based time super-sampling of turbulent flow field sequences. *Phys. Rev. Fluids*, 10(8):084901, 2025.

A. Towne, O. T. Schmidt, and T. Colonius. Spectral proper orthogonal decomposition and its relationship to dynamic mode decomposition and resolvent analysis. *J. Fluid Mech.*, 847:821867, 2018. doi:10.1017/jfm.2018.283.

P. J. Schmid. Dynamic mode decomposition of numerical and experimental data. *J. Fluid Mech.*, 656:528, 2010. doi:10.1017/S0022112010001217.

M. A. Mendez, M. Balabane, and J.-M. Buchlin. Multi-scale proper orthogonal decomposition of complex fluid flows. *J. Fluid Mech.*, 870:9881036, 2019. doi:10.1017/jfm.2019.212.

E. Kaiser, B. R. Noack, L. Cordier, A. Spohn, M. Segond, M. Abel, G. Daviller, J. Östh, S. Krajnovi, and R. K. Niven. Cluster-based reduced-order modelling of a mixing layer. *J. Fluid Mech.*, 754:365414, 2014. doi:10.1017/jfm.2014.355.

H. Li, D. Fernex, R. Semaan, J. Tan, M. Morzyski, and B. R. Noack. Cluster-based network model. *J. Fluid Mech.*, 906:A21, 2021. doi:10.1017/jfm.2020.785.

D. Fernex, B. R. Noack, and R. Semaan. Cluster-based network modelingFrom snapshots to complex dynamical systems. *Sci. Adv.*, 7(25):eabf5006, 2021.

N. Deng, B. R. Noack, M. Morzyński, and L. R. Pastur. Cluster-based hierarchical network model of the fluidic pinball–cartographing transient and post-transient, multi-frequency, multi-attractor behaviour. *J. Fluid Mech.*, 934: A24, 2022.

C. Hou, N. Deng, and B. R. Noack. Trajectory-optimized cluster-based network model for the sphere wake. *Phys. Fluids*, 34(8):085110, 08 2022.

C. Hou, N. Deng, and B. R. Noack. Dynamics-augmented cluster-based network model. *J. Fluid Mech.*, 988:A48, 2024. doi:10.1017/jfm.2024.428.

A. Colanera and L. Magri. Towards extreme event prediction of turbulent flows with quantized local reduced-order models. *arXiv preprint arXiv:2511.04586*, 2025.

R. Geelen and K. Willcox. Localized non-intrusive reduced-order modelling in the operator inference framework. *Philos. Trans. R. Soc. A.*, 380(2229):20210206, 2022.

N. Deng, B. R. Noack, L. R. Pastur, G. Y. Cornejo Maceda, and C. Hou. Cluster globally, model locally: clusterwise modeling of nonlinear dynamics. *Acta Mech. Sin.*, 41(8):324545, 2025.

I.-G. Farcas, R. P. Gundevia, R. Munipalli, and K. E. Willcox. Domain Decomposition for Data-Driven Reduced Modeling of Large-Scale Systems. *AIAA J.*, 62(11):4071–4086, 2024.

W. Xu, Z. Kang, T. Yu, C. Liang, J. Zhang, and W. Bao. Partial proper orthogonal decomposition: Numerical applications and comparisons. *Phys. Fluids*, 37(5):056121, 05 2025.

M. Bergmann, A. Ferrero, A. Iollo, E. Lombardi, A. Scardigli, and H. Telib. A zonal Galerkin-free POD model for incompressible flows. *J. Comput. Phys.*, 352:301–325, 2018. ISSN 0021-9991. doi:10.1016/j.jcp.2017.10.001.

L. Gkimisis, N. Aretz, M. Tezzele, T. Richter, P. Benner, and K. E. Willcox. Non-intrusive reduced-order modeling for dynamical systems with spatially localized features. *Comput. Methods Appl. Mech. Eng.*, 444:118115, 2025. ISSN 0045-7825. doi:10.1016/j.cma.2025.118115.

A. D. Jagtap and G. E. Karniadakis. Extended physics-informed neural networks (xpinn): A generalized space-time domain decomposition based deep learning framework for nonlinear partial differential. *Commun. Comput. Phys.*, 28(5):20022041, Nov. 2020. doi:10.4208/cicp.OA-2020-0164. URL <https://global-sci.com/index.php/cicp/article/view/6911>.

Z. Hu, A. D. Jagtap, G. E. Karniadakis, and K. Kawaguchi. When do extended physics-informed neural networks (XPINNs) improve generalization? *SIAM J. Sci. Comput.*, 44(5):A3158–A3182, 2022. doi:10.1137/21M1447039.

B. Li, Z. Yang, X. Zhang, G. He, B.-Q. Deng, and L. Shen. Using machine learning to detect the turbulent region in flow past a circular cylinder. *J. Fluid Mech.*, 905:A10, 2020. doi:10.1017/jfm.2020.725.

J. L. Callahan, J. V. Koch, B. W. Brunton, J. N. Kutz, and S. L. Brunton. Learning dominant physical processes with data-driven balance models. *Nat. Commun.*, 12:1016, 2021. doi:10.1038/s41467-021-21331-z.

K.-E. Otmani, G. Ntoukas, O. A. Mariño, and E. Ferrer. Toward a robust detection of viscous and turbulent flow regions using unsupervised machine learning. *Phys. Fluids*, 35(2):027112, 02 2023.

Kheir-Eddine Otmani, Andrés Mateo-Gabín, Gonzalo Rubio, and Esteban Ferrer. Accelerating high order discontinuous galerkin solvers through a clustering-based viscous/turbulent-inviscid domain decomposition. *Eng. Comput.*, 41:949964, 2025. doi:10.1007/s00366-024-02062-3.

A. Parente, J. C. Sutherland, L. Tognotti, and P. J. Smith. Identification of low-dimensional manifolds in turbulent flames. *P. Combust. Inst.*, 32(1):1579–1586, 2009.

N. Kambhatla and T. K. Leen. Dimension reduction by local principal component analysis. *Neural Comput.*, 9(7): 1493–1516, 1997.

E. Muñoz, H. Dave, G. D’Alessio, G. Bontempi, A. Parente, and S. Le Clainche. Extraction and analysis of flow features in planar synthetic jets using different machine learning techniques. *Phys. Fluids*, 35(9):094107, 09 2023. ISSN 1070-6631. doi:10.1063/5.0163833.

J. B. Tenenbaum, V. de Silva, and J. C. Langford. A global geometric framework for nonlinear dimensionality reduction. *Science*, 290(5500):2319–2323, 2000.

N. Deng, B. R. Noack, M. Morzyński, and L. R. Pastur. Low-order model for successive bifurcations of the fluidic pinball. *J. Fluid Mech.*, 884:A37, 2020. doi:10.1017/jfm.2019.959.

G. Y. Cornejo Maceda, Y. Li, F. Lusseyran, M. Morzyński, and B. R. Noack. Stabilization of the fluidic pinball with gradient-enriched machine learning control. *J. Fluid Mech.*, 917:A42, 2021. doi:10.1017/jfm.2021.301.

L. Franceschelli, C. E. Willert, M. Raiola, and S. Discetti. An assessment of event-based imaging velocimetry for efficient estimation of low-dimensional coordinates in turbulent flows. *Exp. Therm. Fluid Sci.*, 164:111425, 2025.

E. Farzamnik, A. Ianiro, S. Discetti, N. Deng, K. Oberleithner, B. R. Noack, and V. Guerrero. From snapshots to manifolds—a tale of shear flows. *J. Fluid Mech.*, 955:A34, 2023.

L. Marra, G. Y. Cornejo Maceda, A. Meilán-Vila, V. Guerrero, S. Rashwan, B. R. Noack, S. Discetti, and A. Ianiro. Actuation manifold from snapshot data. *J. Fluid Mech.*, 996:A26, 2024. doi:10.1017/jfm.2024.593.

R. W. Floyd. Algorithm 97: shortest path. *Commun. ACM*, 5(6):345–345, 1962.

W. S. Torgerson. Multidimensional scaling: I. theory and method. *Psychometrika*, 17(4):401–419, 1952.

D. Arthur and S. Vassilvitskii. k-means++: The advantages of careful seeding. In *Proceedings of the Eighteenth Annual ACM-SIAM Symposium on Discrete Algorithms*, SODA '07, page 10271035, USA, 2007. Society for Industrial and Applied Mathematics. ISBN 9780898716245.

M. C. Brindise and P. P. Vlachos. Proper orthogonal decomposition truncation method for data denoising and order reduction. *Exp. Fluids*, 58(4):28, 2017.

B. Protas, B. R. Noack, and J. Östh. Optimal nonlinear eddy viscosity in galerkin models of turbulent flows. *J. Fluid Mech.*, 766:337–367, 2015.

B. R. Noack, K. Afanasiev, M. Morzyński, G. Tadmor, and F. Thiele. A hierarchy of low-dimensional models for the transient and post-transient cylinder wake. *J. Fluid Mech.*, 497:335363, 2003. doi:10.1017/S0022112003006694.

C. Bogey and C. Bailly. Large eddy simulations of transitional round jets: influence of the reynolds number on flow development and energy dissipation. *Phys. Fluids*, 18(6), 2006.

H. Fellouah, C. G. Ball, and A. Pollard. Reynolds number effects within the development region of a turbulent round free jet. *Int. J. Heat Mass Transf.*, 52(17-18):3943–3954, 2009.

J. Mi, M. Xu, and T. Zhou. Reynolds number influence on statistical behaviors of turbulence in a circular free jet. *Phys. Fluids*, 25(7), 2013.

F. Scarano and P. Moore. An advection model to increase the time-resolution of piv time-series. In *Proceedings of 15th international symposium on applications of laser techniques to fluid mechanics, Lisbon*, 2010.

C. G. Ball, H. Fellouah, and A. Pollard. The flow field in turbulent round free jets. *Prog. Aerosp. Sci.*, 50:1–26, 2012.

S. L. Brunton, J. L. Proctor, and J. N. Kutz. Discovering governing equations from data by sparse identification of nonlinear dynamical systems. *Proc. Natl. Acad. Sci.*, 113(15):3932–3937, 2016a.

S. L. Brunton, J. L. Proctor, and J. N. Kutz. Sparse identification of nonlinear dynamics with control (SINDYc). *IFAC-PapersOnLine*, 49(18):710–715, 2016b.

B. Peherstorfer and K. E. Willcox. Data-driven operator inference for nonintrusive projection-based model reduction. *Comput. Methods Appl. Mech. Eng.*, 306:196–215, 2016.

B. Kramer, B. Peherstorfer, and K. E. Willcox. Learning nonlinear reduced models from data with operator inference. *Annu. Rev. Fluid Mech.*, 56(1):521–548, 2024.